Charles University in Prague

Faculty of Mathematics and Physics

MASTER'S THESIS

Jan Kubát

Photoelectric spectroscopy of deep electronic levels in high-resistivity CdTe

Institute of Physics of Charles University

Thesis supervisor: Doc. Ing. Jan Franc DrSc.

Specialization: Physics - Optics and Optoelectronics

2006

Acknowledgements

I hereby state that I have written this master's thesis by myself using only the cited references. I agree to lend it

Prague, 18 April 2006   Jan Kubát

Contents:

Abstract: CdTe is one of the most interesting X-ray and γ-ray detectors' material. This work deals with influence of deep levels to photoelectric properties of CdTe. PICTS, Lux-Ampere and spectral dependences measurements at room temperature and low temperature 10K were performed on one undoped and several variously doped (Cl, Sn and Ge) samples and applied electrical fields up to $800V.cm^{-1}$. Experimental setups are introduced. Room temperature numerical solution of sample photoelectrical properties for typical midgap level using drift-diffusion and Poisson equation was performed and results are discussed. The experimentally observed slopes of Lux-ampere characteristics and energy shifts of the main photoconductivity peak with the applied voltage are explained based on a model of screening of electric field by charge accumulated on deep levels. Finally comparison with acquired experimental data is performed yielding estimates of maximum total concentration of deep levels in the samples.

1   Introduction

The interest in non-cooled and portable spectrometric X and gamma-ray detectors increased remarkably in the last years. There are two reasons for this development:
1.Medical applications developed as a result of more strict demands on secure radiation dose and a necessity to improve image resolution have clearly shown, that semiconductor detectors having ability to use advanced integration technology exhibit a key device for mapping of human organs. 2. Possible terrorist attacks represent huge risks due to a possible application of a "dirty" nuclear bomb. Only a sufficiently dense and sensitive monitoring system based on semiconducting detectors in places, where large amounts of people are concentrated, can remove this type of risk. The state-of–the art in the area of semiconducting detectors specified above is characterized by the fact, that dominating materials are bulk CdTe and CdZnTe [1.] prepared by high pressure Bridgman (HPB) or traveling heater method (THM). The main crystal producers are concentrated in USA (eV Products, Saxonburg, PA), Japan (Nikko), France (LETI, Eurorad) and Canada (Redlen). The progress in quality of detectors was in recent years achieved mainly due to improvements in electronic parts of detectors and detector design [2.]. The crystallinity and photoelectric properties of crystals stagnate and the yield of material with sufficient quality remains relatively low, which causes high detector costs. Inhomogeneity of the CZT grown by HPB remains a problem. Up to 25% of the material is lost due to cracks, but more substantial part of it is not suitable for application due to inclusions, grain boundaries, twins, Zn precipitates, dislocations, etc [3.]. These defects can act as sites for the impurities and native defects segregation. This phenomenon deteriorates significantly the condition of a strong compensation in the working volume of material. Although spectrometric CdTe and CdZnTe detectors are available on the market (Amptec, eV Products, Imarad), inhomogeneites in HPB grown CdZnTe crystals and small diameter of CdTe:Cl crystals prepared by travelling heater method THM method results in necessity to fabricate detector arrays by pixelating instead of using technologies of microelectronics [4.].

2   The goal of the project

One of the main areas to be addressed in order to improve the state-of-the art of semiinsulating crystals is the mechanism of compensation of shallow defects resulting in a high resistivity state, because despite a long-term effort to investigate the structure of defects in CdTe and CdZnTe, which was summarized in several reviews (e.g. [5.]), this mechanism is not fully clear. The goal of this diploma project is to perform analysis of photoelectric properties of high resistivity samples doped with various dopants, to evaluate the possibility of preliminary testing of the material quality from steady-state photoconductivity measurements and to contribute to the clarification of the compensation mechanism.

3 Basic characteristics of CdTe

CdTe has been known for a long time as a promising semiconductor with applications as gamma and x-ray detectors. The lattice match and chemical compatibility between CdZnTe and various compositions of HgCdTe make CdZnTe prime candidate as substrate material for HgCdTe epitaxy. CdTe is also one of the leading semiconducting materials in photovoltaic research. It demonstrated more than 15% efficiency in various laboratories and more than 10% efficiency measurement in industrial applications.

Many physical properties are controlled to some extent by the relative position of the energy levels within forbidden gap associated with their native defects or impurities. Both energy levels close to the band edges and deep levels play an important role in determining the electrical properties of the material. It was observed that majority of these defect levels form several bands in the band gap with each band consisting of many discrete levels. Even though it is difficult to draw a clear line to distinguish between shallow and deep levels, we considered the trap levels having activation energy more than 0.2eV as a deep level and those levels with energies lower than 0.2eV as a shallow level.

3.1 Not intentionally doped CdTe:

Not intentionally CdTe and CdZnTe samples, prepared on the Te part of the phase diagram (low Cd pressure), have normally p-type conductivity with carrier concentrations typically about 10^{15}cm^{-3}. CdTe in uncompensated form is a low-resistivity semiconductor due to the intrinsic defects and residual impurities. In undoped CdTe we can observe several native defects. The predominant defects are cadmium vacancy acting as singly (V_{Cd}) and doubly ionized (V_{Cd}^{2-}) acceptor levels or interstitial Cd_I, (for crystals grow on the cadmium site of the phase diagram). The complex defects formed due to doubly ionized cadmium vacancy and impurity donor atoms from group III and VII behave as singly ionized shallow acceptors and neutral donors The high resistivity of undoped CdTe indicates relatively few electrically active impurities. Overview of the level energies calculated from first principles is shown in **Table I** and illustratively in **Fig. 3-1**.

Table I - The ab initio calculated energies of main native defects in CdTe [6].

Defect	$E_{d(a)}^1$ (eV)	$E_{d(a)}^2$ (eV)
Cd_I	0 [7.] 0.21 [8.]	0.17 [7.] 0.36 [8.]
V_{Cd}	0.2 [7.]	0.47 [9.]
Te_{Cd}	$0.9\,E_g$ [6.]	E_g [6.]

A graphical scheme of levels is presented too.

E_C ───────────────────

Cd_I - - - - - - - - - - - - - - - E_C-0.17 eV
E_C-0.21 eV

Cd_I - - - - - - - - - - - - - - - E_C-0.36 eV

V_{Cd} - - - - - - - - - - - - - - - E_V+0.47 eV

V_{Cd} - - - - - - - - - - - - - - - E_V+0.2 eV

E_V ───────────────────
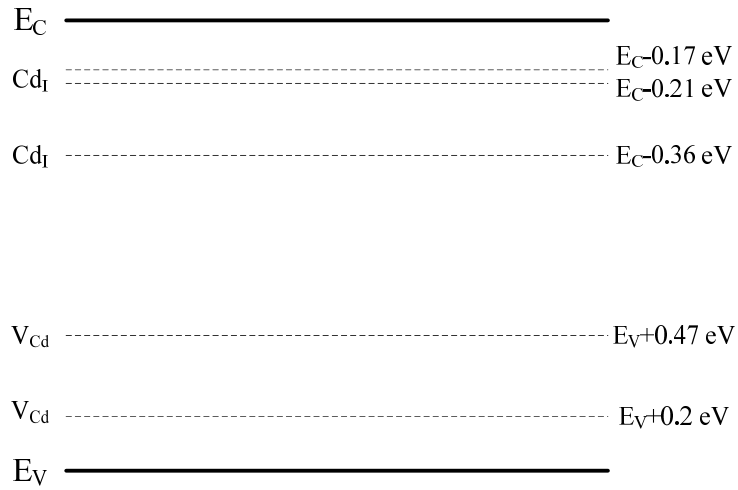
Fig. 3-1
Forbidden band in CdTe with energy levels of principal native defects

There were observed other levels in undoped samples too. They are ascribed to other native defects or their complexes List of levels found in undoped samples is shown in the following table. Main native defects presented in samples are vacancy of cadmium V_{Cd}, tellurium on cadmium site Te_{Cd}, intrinsic tellurium Te_I, complex of Te_{Cd} and V_{Cd}, vacancy of tellurium V_{Te} and intrinsic cadmium Cd_I.

Table II - Energies of native defects in CdTe

Defect	Energy [eV]	Capture cross-section [cm^2]	Donor / Acceptor	Method	Reference
V_{Cd}	<0.047		Acceptor	Photo-EPR	[10.]
V_{Cd}	0.100		Acceptor	DLTS, PICTS	[11.]
V_{Cd}	0.100		Acceptor	Theory	[12.]
V_{Cd}	0.200		Acceptor	Theory	[13.]
V_{Cd}	0.210		Acceptor	TEES	[14.]
V_{Cd}	0.400		Acceptor	DLTS, PICTS	[11.]
V_{Cd}	0.430		Acceptor	TEES	[15.]
V_{Cd}	0.730		Donor	TEES	[14.]
V_{Cd}	0.760		Acceptor	DLTS, PICTS	[11.]
V_{Cd}	0.78	4×10^{-13}	Acceptor	PICTS	[16.], [17.]
V_{Cd}	0.800		Acceptor	Theory	[13.]
Te_{Cd}	0; 0.4		Donor	Theory	[13.]
Te_I			Donor	Theory	[13.]
Te_{Cd}-V_{Cd}			Neutral	Theory	[13.]
V_{Te}	1.400		Donor	Photo-EPR	[18.]
V_{Te}	1.100		Donor	DLTS, PICTS	[11.]
V_{Te}	0.400		Donor	Theory	[13.]
V_{Te}	0.500	1×10^{-16}	Donor	Theory	[12.], [19.]
Cd_I	0.640	4×10^{-12}	Donor	DLTS, PICTS	[11.], [17.]
Cd_I	0.540		Donor	PICTS	[20.]
Cd_I	0.500		Donor	Theory	[12.]
Cd_I	0; 0.2		Donor	Theory	[13.]
Unknown	0.250	$2\text{-}3\times10^{-19}$			[19.]
Unknown	0.240	$2\text{-}6\times10^{-17}$		DLTS	[21.]
Unknown	0.880	1.2×10^{-12}			[19.]

Various methods were used to levels detection: Photo-EPR (photo electron paramagnetic resonance), DLTS (deep level transient spectroscopy), PICTS (photo induced current transient spectroscopy), TEES (thermal emission electron spectroscopy), PL (photoluminescence), ODMR (optically detected magnetic resonance), SPS (surface plasmon spectroscopy), CPM (constant photocurrent method), TSC (Thermally stimulated current spectroscopy), Hall (Hall measurement) or TDL (tunable diode laser spectroscopy).

3.2 Intentionally doped CdTe:

There are two main manners to doping samples
1) Doping with transition metal elements
2) Doping with elements from groups I, III, IV, and VII
It was experimentally confirmed that both types doping can lead to high resistivity material [5.].

In samples doped with transition metals like vanadium or titanium one can obtain high resistivity due to presence of deep level in the middle of the band gap.

Table III - Energies of transition metal elements in CdTe

Dopant	Energy [eV]	Donor / Acceptor	Experimental method	Reference
Ag	0.108	Acceptor	PL	[22.]
Au	0.263	Acceptor	PL	[23.]
Co	1.250	Acceptor	EPR, ODMR,PL	[24.]
Cr	1.340	Acceptor	EPR, ODMR,PL	[25.]
Cu	0.146	Acceptor	PL	[24.]
Cu	0.360	Acceptor	PICTS	[26.]
Cu	0.370	Acceptor	PICTS	[20.]
Fe	0.150	Acceptor	SPS	[27.]
Fe	0.200	Acceptor	CPM	[10.]
Fe	0.350	Acceptor	EPR, ODMR,PL	[28.]
Fe	0.430	Acceptor	TSC	[29.]
Fe	1.450	Donor	Photo-EPR	[30.]
Mn	0.050	Donor	Hall	[31.]
Mn	0.730	Donor	Hall	[30.]
Ni	0.760	Donor	CPM	[10.]
Ni	0.920	Acceptor	EPR, ODMR,PL	[28.]
Sc	0.011	Donor	PL	[32.]
Ti	0.730	Donor	PL, TDH	[32.]
Ti	0.830	Donor	DLTS	[33.]
V	0.510	Acceptor	TSC	[29.]
V	0.670	Donor	Photo-EPR	[34.]
V	0.740	Acceptor	Theory	[35.]
V	0.950	Donor	DLTS	[36.]

Doping with donors having deep, near midgap levels (Sn_{Cd}, Ge_{Cd}) results in high resistivity [37, 38 and references therein].
Doping with shallow donors (Al, In occupy Cd site, Cl occupies Te site) or acceptor like P which occupies Te site should decrease the resistivity of the sample, in spite of this high resistivity is often observed. A theoretical model explaining the role of shallow donors in formation of high resistivity state, when a midgap level with a very low concentration $N_{deep} < 10^{13} cm^{-3}$ is present, was recently proposed [39.] The model is based on processes of self-compensation and

precipitation of Cd vacancies in CdTe doped with shallow donors (In, Cl) during cooling to room temperature.

Energy levels related to major impurities of elements from groups I, III, IV, and VII and their complexes with native defects are shown in **Table IV**.

Generally there is little information about concentration of deep centers in the literature. Concentrations of deep levels were studied in low-resistivity CdTe by DLTS. The measured concentrations vary in the interval 8.5×10^{12}-$6 \times 10^{14} cm^{-3}$ in most cases [40, 41, and 42.]. It is however difficult to transfer this information to high resistivity samples. The process of formation and reaction of defects due to introduction of dopants (self compensation, precipitation, complex formation) can influence the defect concentration substantially.

Table IV - Energies of elements from groups I, III, IV, and VII in CdTe

Dopant	Energy [eV]	Capture cross-section	Donor / Acceptor	Experimental method	Reference
Al	0,014		Donor	PL	[43.]
As	0,092		Acceptor	PL	[44.]
Cl	0,014		Donor		[10.]
Cl	0,015		Donor	PL	[43.]
Cl-DX1	0,220		Donor	Theory	[45.]
Cl-DX2	0,470		Donor	Theory	[45.]
Cl-DX3	0,210		Donor	Theory	[45.]
Cl-VCd	0,120		Acceptor	PL, ODMR	[46.]
F	0,014		Donor	PL	[43.]
Ga	0,014		Donor	PL	[43.]
Ge	0,730		Acceptor	Photo-EPR	[32.]
Ge	0,950		Donor	Photo-EPR	[28.]
In	0,014		Donor	PL	[43.]
In	0,220	8.6×10^{-13}	Acceptor	DLTS	[21.]
In	0,230	2×10^{-15}	Acceptor	QTS	[17.]
In	0,230	$3\text{-}4 \times 10^{-13}$	Acceptor		[47.]
In	0,280	2×10^{-13}	Acceptor		[47.]
In	0,320	2×10^{-14}	Acceptor	QTS	[17.]
In	0,340	$1\text{-}5.5 \times 10^{-13}$	Acceptor	DLTS	[21.]
In	0,340	1×10^{-13}	Acceptor		[47.]
In	0,380	4.9×10^{-14}	Acceptor		[47.]
In	0,470	2×10^{-15}	Acceptor		[47.]
In	0,580	2×10^{-15}	Acceptor	DLTS	[21.]
In	0,680	3×10^{-13}	Acceptor	DLTS	[21.]
In	0,800	5×10^{-13}	Acceptor	QTS	[17.]
In, undoped	0,210	5×10^{-14}	Acceptor	DLTS	[21.]
In, undoped	0,280	6.5×10^{-13}	Acceptor	DLTS	[21.]
In, undoped	0,380	3×10^{-9}	Acceptor	DLTS	[21.]
In, undoped	0,460	4×10^{-14}	Acceptor	DLTS	[21.]
In, undoped	0,740	$1\text{-}6 \times 10^{-14}$	Acceptor		[47.]
In, undoped	0,860	2×10^{-12}	Acceptor	DLTS	[21.]
Li	0,058		Acceptor	PL	[48.]
N	0,056		Acceptor	PL	[44.]
Na	0,059		Acceptor	PL	[48.]
P	0,068		Acceptor	PL	[44.]
Pb	1,280		Donor	Photo-EPR	[28.]
Sn	0,380	0.9×10^{-13}	Acceptor	QTS	[17.]
Sn	0,430	4×10^{-14}	Donor	QTS	[17.]
Sn	0,510	1×10^{-14}	Acceptor	QTS	[17.]
Sn	0,850		Donor	Photo-EPR	[28.]
Sn	0,890	5×10^{-12}	Donor	QTS	[17.]
Sn	0,900		Donor	DLTS	[42.]

4 Theory

4.1 *Shockley-Read-Hall model*

The band diagram of the perfect single crystal semiconductor consists of a valence band and a conduction band separated by the forbidden band. When the periodicity of the single crystal is perturbed by foreign atoms or crystal defects, discrete energy levels are introduced into the band gap. Each energy level created from such defects can be represented by energy E_T and concentration of centers N_T. The Shockley-Read-Hall statistic model for generation-recombination of electron-hole pairs in crystal semiconductors is based on trapping mechanism of electrons on the generation-recombination centers in the forbidden band (deep-level impurities). They can act as recombination centers when there are excess carriers in the semiconductor and as generation centers when the carrier density is below its equilibrium value. These centers can be obtained due to metallic impurities or as the result of the crystal imperfections (dislocations, precipitates, vacancies or interstitials), most of them are undesirable [49, 50.].

Basic preconditions of SRH model are:
1) free charge carriers can be only described with concentration n and mid-thermic velocity
2) all crossings are immediate processes
3) parameters of trapping centers do not depend on state of surrounding system and correspond to equilibrium states

The transfer of electrons from the valence band to the conduction band is referred to the generation of electron-hole pairs (or pair-generation process), since not only a free electron is created in the conduction band, but also a hole in the valence band which can contribute to the charge current. The inverse process is thermal recombination of electron-hole pairs. A third event, which is neither recombination nor generation, is the trapping event. In either case a carrier (electron or hole) is captured and subsequently emitted back to the band from which came. Only one of the two bands and the center participate. The basic mechanisms are illustrated in **Fig. 4-1**.
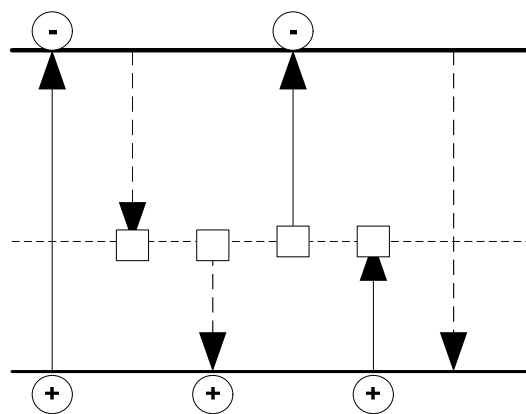

Fig. 4-1
Bandgap model with six basic processes of recombination with one deep level
(1-generation of e^-h^+ pair, 2-capture of electron on trap, 3-capture of hole on trap,
4-excitation of electron from trap, 5-excitation of hole from trap, 6- bandgap recombination)

Generally the electron emission rate for centers in the upper half of the band gap is much higher than the hole emission rate. This is in contrast with emission rates for centers in the lower half of the band gap. For most centers one emission rate dominates, and the other can frequently be neglected. The concentration of G-R centers occupied by electrons n_T, and holes p_T must equal the total concentration of centers N_T.

$$n_t + p_t = N_t \tag{1}$$

We define some quantities for model description
- S_n – capture coefficient for electrons
- S_p – capture coefficient for holes
- E_t – energy of centre
- N_t – concentration of centers
- n_t – concentration of electrons on centers

According to capture coefficient we distinguish
- $S_n \approx S_p$ – recombination centre
- $S_n \approx S_p$ – trap for electrons
- $S_n \approx S_p$ – trap for holes

Relaxation time of free electrons in equilibrium state on trap is defined as

$$\tau_n = \frac{1}{S_n v_n (N_t - n_t)}, \tag{2}$$

where v_n (v_p) is electron (hole) thermal velocity.

Change of concentration of electrons in conduction band and holes in valence band is fully described by the following equations:

$$\frac{dn}{dt} = G + S_n v_n n_t n_1 - S_n v_n n (N_t - n_t), \tag{3}$$

$$\frac{dp}{dt} = G + S_p v_p (N_t - n_t) p_1 - S_p v_p p n_t, \tag{4}$$

$$\frac{dn}{dt} = S_n v_n (N_t - n_t) - S_n v_n n_t n_1 + S_p v_p (N_t - n_t) p_1 - S_p v_p p n_t, \tag{5}$$

$$\Delta n + \Delta n_t = \Delta p \tag{6}$$

In case that carries are not in equilibrium state we must calculate carriers´ relaxation time according to Shockley-Read relation

$$\tau = \tau_{p_0} \frac{n_0 + n_1 + \Delta n}{n_0 + p_0 + \Delta n} + \tau_{n_0} \frac{p_0 + p_1 + \Delta p}{n_0 + p_0 + \Delta n} \tag{7}$$

Where τ_{n0} and τ_{p0} correspond to lifetime for electrons (holes) to totally empty (totally full of electrons) level.

4.2 Drift-diffusion and Poisson equations

The principles of the simulation of the photoconductivity in homogeneous planar sample with a thickness L biased by a voltage U and characterized by Fermi energy E_F, which yields equilibrium electron and hole density before illumination n_0 and p_0, respectively, will be reviewed in the following paragraph. The considered deep level with density N_{deep} is described by ionization energy E_{deep}, electron and hole capture cross sections S_n and S_p. Note that the character of the deep level (charge, donor or acceptor) is not directly present in the theoretical forms.
The description of the free carrier's motion in the sample without spatial charge is based on the self-consistent steady state solution of electron and hole drift-diffusion equations.

$$j_n = e\mu_n n\vec{E} + \mu_n k_0 T\nabla n + \mu_n k_0 n\nabla T \tag{8}$$

The first part of the equation is related with drift in electrical field in response to changes in the band-edge energy and changes in the electrostatic potential. The second part is related with diffusion is due to the difference in the charge carrier's concentration. Equivalent form for holes can be written. T is carrier temperature and the mobility of the free carriers is defined as

$$\mu_{n,p} = \frac{e}{m_{n,p}^*}\tau \tag{9}$$

With the assistance of effective mass of free electrons m_e^* and relaxation time τ

The effect of space charge to the electric field distribution and carrier transport through the sample is evaluated by solving the Poisson equation. The electron and hole equilibrium in the steady photoexcited system is described by equations

$$0 = \Phi\alpha e^{-\alpha x} + \mu_n\left[\frac{k_b T}{e}\frac{\partial^2 n}{\partial x^2} + \frac{\partial}{\partial x}\left(\vec{E}n\right)\right] - R, \tag{10}$$

$$0 = \Phi\alpha e^{-\alpha x} + \mu_p\left[\frac{k_b T}{e}\frac{\partial^2 p}{\partial x^2} - \frac{\partial}{\partial x}\left(\vec{E}p\right)\right] - R, \tag{11}$$

where Φ is the photon flux, α is the absorption coefficient, and $\mu_{n(p)}$ is the electron (hole) drift mobility. The Einstein relation $eD=k_b T\mu$ is used to express the drift term with mobility μ. Carrier recombination R is described within the Shockley-Read-Hall model.

$$R = \frac{\gamma_n\gamma_p N_{deep}\left(np - n_0 p_0\right)}{\gamma_n\left(n + n_1\right) + \gamma_p\left(p + p_1\right)}, \tag{12}$$

The capture coefficient is defined by $\gamma_{n(p)} = S_{n(p)} \cdot v_{n(p)}$ with electron (hole) thermal velocity v_n (v_p) and n_1, p_1 are electron and hole densities in case of Fermi level being set to E_{deep}. The electric field

$$\vec{E} = -\frac{\partial \varphi}{\partial x} , \tag{13}$$

and the electrochemical potential φ are obtained solving the Poisson equation

$$\frac{\partial^2 \varphi}{\partial x^2} = -\frac{\rho}{\varepsilon} , \tag{14}$$

with boundary conditions $\varphi(0)=0$ and $\varphi(L)=U$. The charge density ρ is given by the change of the band and level occupation

$$\rho = e \left(p - p_0 - n + n_0 - n_t + n_{t0} \right) , \tag{15}$$

where n_t and n_{t0} defines deep level occupation,

$$n_t = \frac{N_{deep} \left(\gamma_n n + \gamma_p p_1 \right)}{\gamma_n \left(n + n_1 \right) + \gamma_p \left(p + p_1 \right)} , \tag{16}$$

$$n_{t0} = \frac{N_{deep}}{1 + e^{\left(E_{deep} - E_F \right)/k_b T}} , \tag{17}$$

The variation of occupation of shallow levels is neglected.
Equilibrium carrier density $n(0)=n(L)=n_0$ and $p(0)=p(L)=p_0$ is used as a boundary condition and Eqs. (11),(12) are solved numerically by an iterative method. Both dark current I_0 and photocurrent I_{ph} are constant through the sample and the photocurrent is expressed by

$$I_{ph} = eL \left[\mu_n n(x) + \mu_p p(x) \right] E(x) - e(\mu_n n_0 + \mu_p p_0)U , \tag{18}$$

4.3 PICTS theory

PICTS (photo-induced current transient spectroscopy) is one of the methods used for investigation of deep levels in high-resistivity bulk materials. The method is based on storing and processing data of photocurrent decay after illumination by laser LED diode for various temperatures. In this theory we consider single trapping level configuration and negligible retrapping, which is the ideal model. We assume that period of darkness is long enough so that traps are empty at time of new beam flash. The current $i(t_\infty)$ is thus the dark current. According to the assumption made the current induced by detrapping can be written as

$$i(t) = qAE\mu_p\tau_p p_t(0)\frac{1}{\tau_t}\exp\left(-\frac{t}{\tau_t}\right) + i(t_\infty),$$ (19)

Where $p_t(0)$ is the initial density of filled traps (here holes are considered), μ_p and τ_p are respectively the mobility and recombination lifetime of free holes, q is the electronic charge, E the applied electrical field. The constant A depends on the illumination surface between the electrodes and on the penetration depth of the light. The relaxation time of holes τ_t is related to the depth of the light E_t of the level (with respect to the top of the valence band) and to capture cross section of trap centers S_t by the expression

$$\frac{1}{\tau_t} = S_t v N_v \exp\left(-\frac{E_t}{kT}\right),$$ (20)

Where N_v is the effective density of states in the valence band and v the thermal velocity of the holes. Similar expressions are valid for the case of electrons [51.].

In reality current decay is the sum of more than one exponential. There can be seen three regions of decay in the **Fig. 4-2**.
   a) Rapid decay region corresponds to the carriers released by the traps with large emission cross section – needn't to be the finest as there can be artifacts due to the non-zero cut-off time of the exciting light beam.
   a) Intermediate decay region that is relied to the traps those are in the thermal resonance at the measuring temperature.
   b) A slow decay region corresponds to the carriers by traps with small emission cross-section – Evaluation of this part is often problematic due to interference of the weak signal with the background.
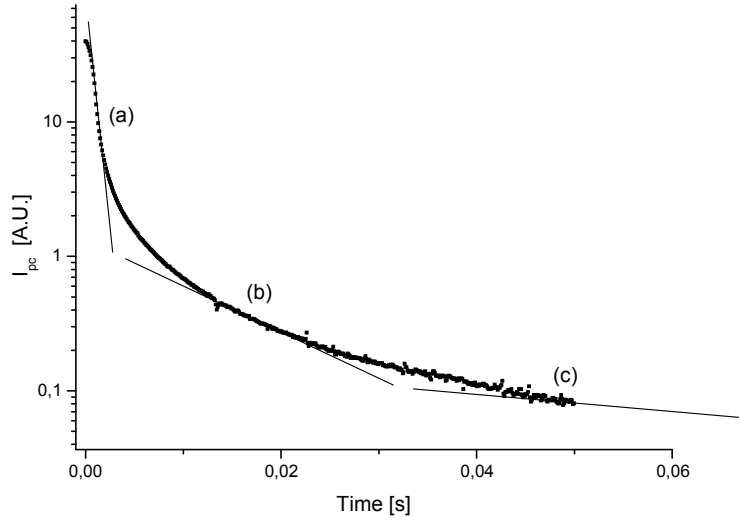
Fig. 4-2

Semilogarithmic plot of a transient signal received from an Au/CdTe contact at 95K

4.3.1 Two-gate methods for PICTS evaluation

The basic two-gate method for transient's evaluation consists of plotting of the difference

$$\Delta_{12}i(T) = i(t_1) - i(t_2) \tag{21}$$

as a function of temperature, where t_1 and t_2 are two delay times at which the readings are taken from transient. Usually t_2 is chosen large with respect to t_1. After processing we get set of spectra from which we need to get temperature T_m of maximum; they can be expressed as

$$\Delta i_{12}(T_m) = qA\vec{E}\mu_p\tau_p p_t(0)\frac{1}{\tau_m}\frac{t_2 - t_1}{t_2 - t_m}\exp\left(-\frac{t_1}{\tau_m}\right) \tag{22}$$

The dependence of the amplitude of the maximum on the temperature T_m may provide an independent method for determination of the trap parameters.

The important point for using double-gate processing is to make sure, that the initial filling $p_t(0)$ of the traps remains constant over the temperature range of interest. This condition may in principle be fulfilled by using high photo-excitation in order to saturate the traps. One of the most important problems in bulk samples is that the lifetime and possibly the mobility of the thermally released carriers may depend on temperature in a manner, which cannot be expressed in a simple analytical form.

- 16 -

4.3.2 Four gate methods for PICTS evaluation

The way to solve this problem is to compute the ratio $\Delta i_{12}(T)/\Delta i_L(T)$, which means to normalize PICTS signal. The heights of the peaks in a normalized spectrum then reflect the relative concentrations for the various types of traps present in the material.

For data evaluation I used this method (4-gate) PICTS signal processing. The double-gate method has the following drawbacks:
a) It is, in general, not easy to take into account possible thermal variations of mobility and recombination lifetime, especially if the thermally released carriers are not of the same type as the photocarriers.
b) One cannot be sure that $p_t(0)$ remains constant over the whole temperature range.
c) Owing to some uncertainty concerning the presence or not of the $1/\tau_t$ in the pre-exponential factor.

Four-gate processing consist in reading the recordings at four different times t_0, t_1, t_2, t_3 and in computing the ratio

$$Y[\tau_t(T)] = \frac{i(t_1) - i(t_2)}{i(t_0) - i(t_3)},$$ (23)

Where optional parameters $t_1/t_0 = 2$ and $t_2/t_0 = 3$ were fixed for the data processing.

For plotting the Arrhenius diagram it is necessary to compute the relaxation time τ_m for each PICTS spectrum corresponding to the temperatures T_m at which the maximum occurs.

$$\tau_m = \frac{t_2 - t_1}{\ln[(t_2 - t_0)/(t_1 - t_0)]},$$ (24)

Points in Arrhenius diagram ($10^3/T_m$ as x axis, $T_m^2\tau_m$ as y axis) are then interlaid by the linear apparent fit from which we can acquire values of capture cross sections S_t end activation energies of the traps $\Delta E = E_C-E_T$ for electrons and $\Delta E = E_V-E_T$ for holes [51.].
This apparent fit can be expressed by formula

$$y = A + Bx$$ (25)

Activation energies can be computed from equation

$$\Delta E = B.k.10^3$$ (26)

where k is Boltzmann constant. Capture cross sections for electrons and holes are calculated from

$$S_n = \frac{h^3}{\sqrt{96k^2 m_n}} \exp(-A) \qquad (27)$$

$$S_p = \frac{h^3}{\sqrt{96k^2 m_p}} \exp(-A) \qquad (28)$$

where h is Planck constant and m_n, m_p are effective masses of electrons and holes.

4.4 "Tail" model of sublinear dependence of Lx-A characteristics

The classical Rose model [52.] for description of Lux-Ampere characteristics $I_{PC} \sim \Phi^\alpha$ ($0.5 \leq \alpha \leq 1$) assumed that in the dark recombination centers are fully filled with electrons and that the levels in the sample are distributed continuously. Typically Rose assumed exponential distribution of levels in the bandgap [53.]

$$N_t(E) = A \exp\left(-\frac{|E_C - E_t|}{kT_1}\right) \qquad (29)$$

Where A in constant and T_1 is parameter which determines the rate of growth of concentration N_t with energy. We assumed that $S_e \ll S_h$, which means that concentration of excited electrons is much higher then redundant concentration of holes $n \gg p$.
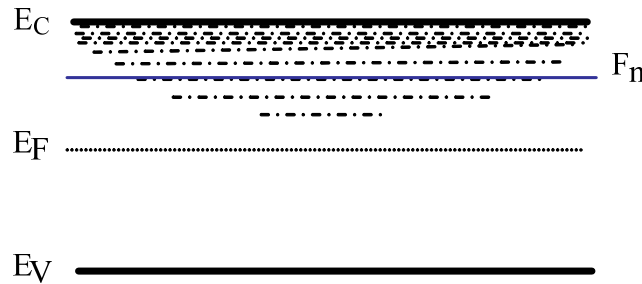
Fig. 4-3
Model of levels according to the Rose model

In case of homogenous illumination is the quasi-Fermi level F_n moved toward the conduction band. With increasing illumination more and more levels N_t become recombination levels. Therefore, the relaxation time of electrons is decreased due to rising concentration of recombination levels.

Number of recombination centers p_R for electrons is corresponding to concentration of levels N_t between Fermi level E_F and quasi-Fermi level F_n.

$$p_R \approx kT_1 N_t(F_n), \qquad (30)$$

Finally we can derive concentration of electrons in conduction band

$$n \approx \left(\frac{N_C^{T/T_1}}{T_1} \right)^{\frac{T_1}{T+T_1}} , \tag{31}$$

the exponent in equation (32) can take value in range 0.5-1, if the parameter T_1 is greater than T.

This model is not able to describe overlinear dependences. It would be necessary to define two types of recombination centers.

In fact, the assumed exponential distribution only needs to be approximated by an exponential form over the range of energies between the dark Fermi level and quasi Fermi levels. Therefore also a discrete level positioned in this energy range can result in sublinear character of Lx-A characteristics in a limited range of incident photon fluxes.

4.5 Screening of electric field

For description of sublinear Lx-A characteristics in crystals with discrete spectra of levels other model was proposed. [36.]. It is based on an assumption of screening of electric field near the illuminated contact due to accumulation of charge on deep levels. The authors assume, that the sample can be divided into two layers – a layer of zero electric field (dead layer) at the illuminated electrode and an active layer (see **Fig. 4-4** zones A and B). The width of the dead layer increases with increased illumination. Electron-hole pairs generated by light in the dead layer move through this region by diffusion. Their number is decreased by recombination. Those which reach the active layer then contribute to photocurrent.
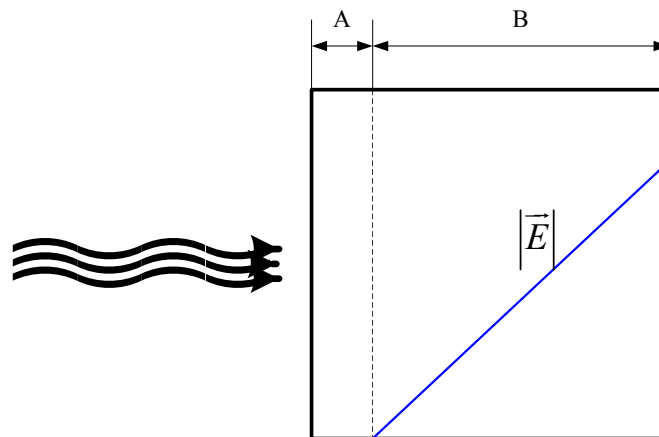
Fig. 4-4
Model of the sample with diffuse and drift parts and charge screening effect

The maximum concentration guaranteeing linear course of lux-ampere characteristics up to current density j calculated based on this model is:

$$N_{deep} = 4\pi\varepsilon_0\varepsilon_r \frac{\mu_p V^2 N_V \exp\left(-\dfrac{\Delta E}{kT}\right)}{j_\phi L^3} + 2\frac{V}{eL}, \tag{32}$$

Where L is sample width, V is applied voltage, σ_ϕ is photon flux.

4.6 The three level model of compensation

The model is trying to describe high resistivity in CdTe samples like an effect of compensation among shallow acceptors, donors and one deep level. According to a classical model without deep level the sample resistivity should be bellow $10^3\Omega$.cm, if the concentration of acceptor and donor impurities is in the range 10^{16}cm^{-3} - 10^{15}cm^{-3}.
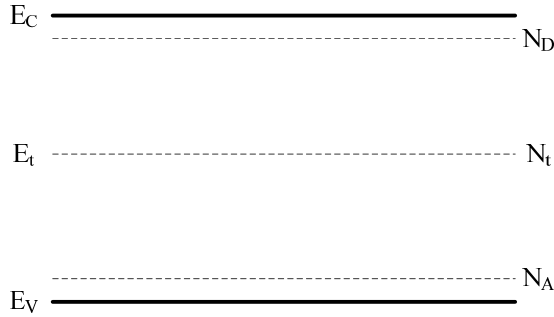
Fig. 4-5
3-level model of compensated semiconductor

It is assumed that that there is the difference between concentration of shallow donors and acceptors

$$N_D < N_A \text{ respectively } N_A < N_D, \tag{33}$$

Then there must be sufficient concentration of deep centers for trapping of free carriers

$$N_{deep} \gg N_A - N_D \text{ respectively } N_{deep} \gg N_D - N_A, \tag{34}$$

According to this model with typical parameters $S_e=1.10^{-15}$cm^2, $N_{deep}=10^{16}$cm^{-3} and using equation (36)

$$\tau_{n,h} = \frac{1}{S_{n,h} v_t N_{deep}} \, , \tag{35}$$

we get for room temperature relaxation time of electrons $\tau_n \sim 10^{-8}$s. Where v_t is thermally speed of electrons. This time is too short for drift of electrons from sample volume to the contacts, if standard operating conditions of detectors are supposed (thickness~1mm, E=1-2kV.cm^{-1}). At the same time it is known, that functioning CdTe and CdZnTe detectors exist. The question therefore arises, how the compensation mechanism in detector-grade crystals works does and what is the real concentration of deep levels pinning the Fermi energy.

4.7 Photocurrent spectra

During most experiments difference from the theoretical absorption edge $\sqrt{E}$ is observed. This is due to Urbach edge bellow energy of the gap E_g and due to growing of absorption coefficient with photon energy. This causes absorption of the light in the front layer of the sample and subsequent decreasing of photocurrent in the bulk sample due to an increased surface recombination. As a result of this a photocurrent peak near the absorption edge is formed [53, 54.].
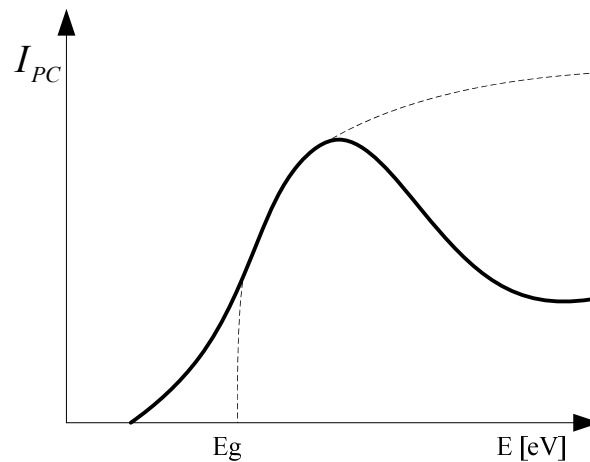
Fig. 4-6
Behavior of photoconductivity dependence on photon energy – dashed line represents theoretical absorption edge

5   Experiment

5.1 Sample preparation

The high-resistivity (10^9-5×10^9 Ωcm) CdTe crystals investigated in this master thesis were prepared by vertical gradient freeze method [55.] and by growth from Te solvent. They were doped by various dopants (Cl, In, Sn). The list of studied samples is given in Table 1. The samples for measurement of photoconductivity had dimensions about 5x5x1.5mm^3. The samples were chemically and mechanically etched in 1% Br-methanol solution prior to contact fabrication. Contacts covering the whole front and back surfaces were fabricated by chemical deposition using of a 0.1% $AuCl_3$ solution applied for 10s. We performed measurement with Fourier spectrometer to obtain transmittance through the sample, covered with and without one contact, in range 700nm to 1100nm. It is apparent, that approximately 1% of the light penetrates through the front contacts to the sample. The drop of the signal at ≈ 1.47eV is caused by absorption of the light in the CdTe.
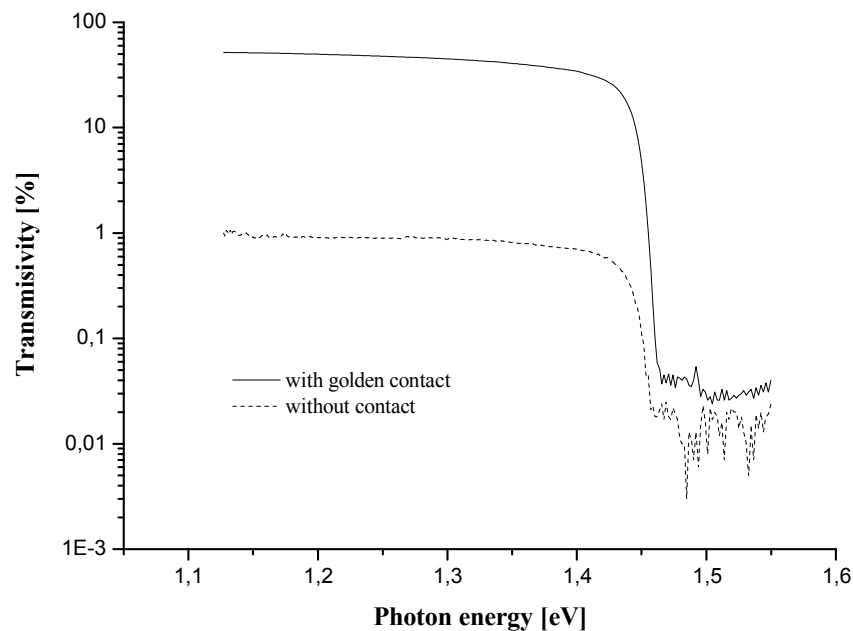
Fig. 5-1
Transmittance through the sample with and without gold layer.

The V-A characteristics of contacts in dark were ohmic with a maximum deviation of 1% from ideal course as is shown in the **Fig. 5-2.** Similar results on high-resistivity CdTe samples were obtained in [56.] too, where linear dependence of I-V characteristics was confirmed up to electric field 3000V/cm.
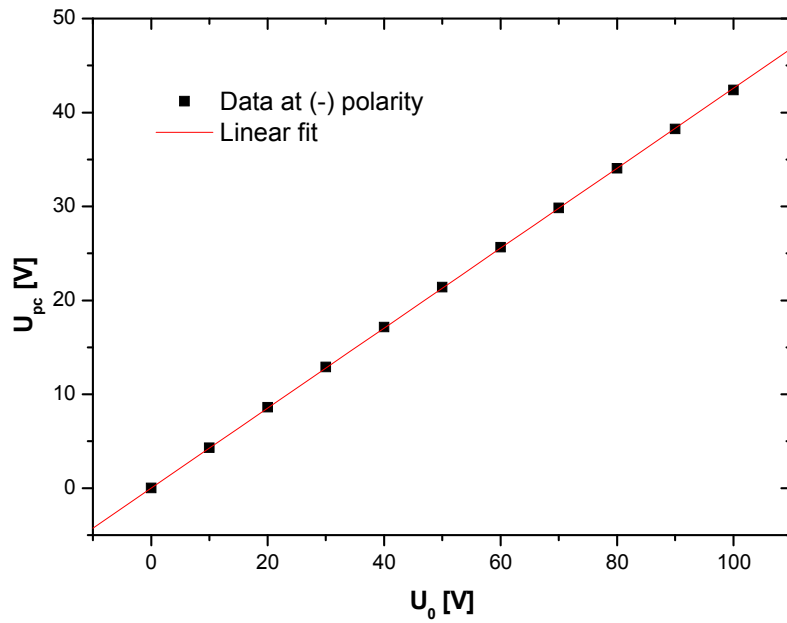
Fig. 5-2
V-V characteristic of Au contact in the dark

5.2 Mounting of the samples

CdTe sample with contacts on front and back sides was fastened to beryllium plate by high heat conductivity paste and then to the cryostat handle with high vacuum grease. The sample Au contacts were then connected to the contacts on the beryllium plate with liquid Ag from where was a connection to contacts in the cryostat. Since the sample was in vertical position during measurement, the beryllium plate had to be fastened to the Cu finger thoroughly before the cryostat was pumped. The setup of the sample in the cryostat is shown in **Fig. 5-3**.

Vacuum grease

Cu handle

Indium

Ag wire

CdTe sample

U_0

Light beam

Lock-In

Glass window

R_C

Au contact

Cryostat

Paste

Beryllium plate
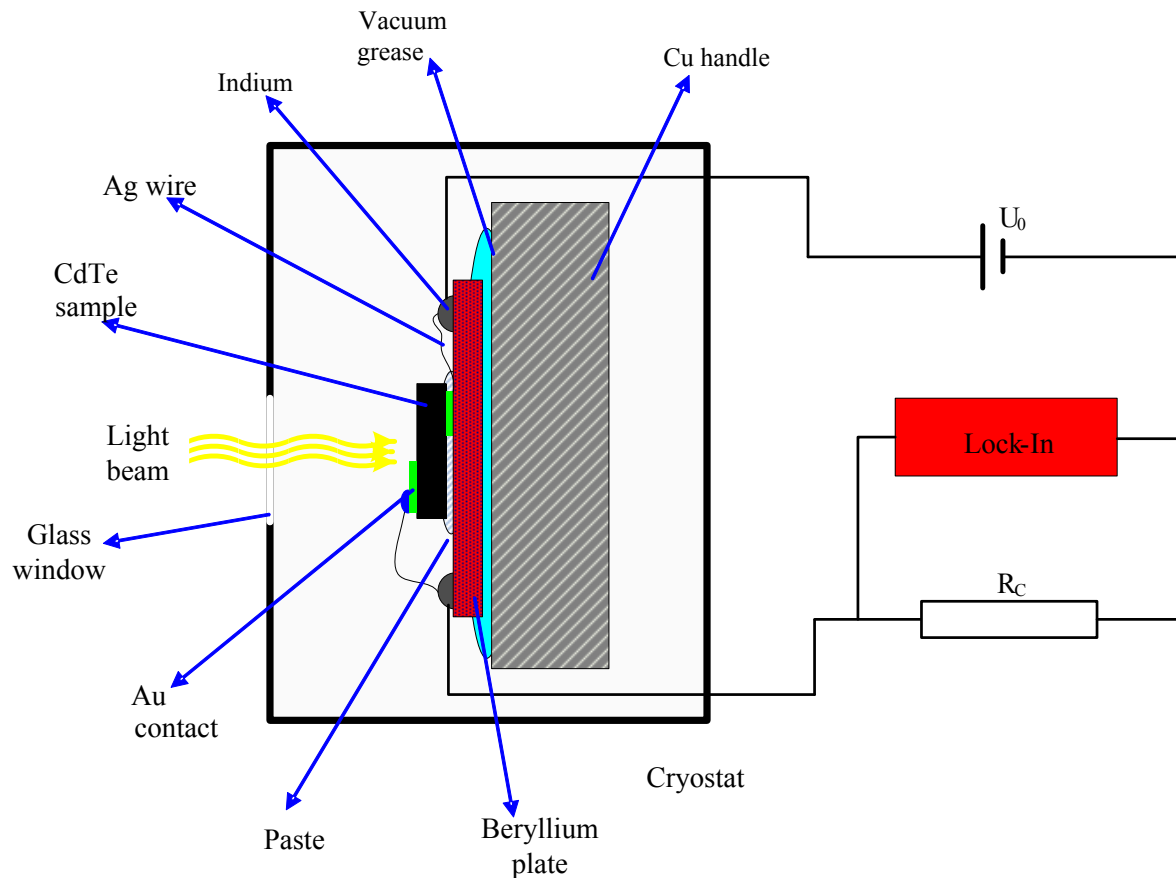
Fig. 5-3
CdTe sample in the cryostat

5.3 Setup with the monochromator

The source of the light we used was a high emission discharge lamp. The light beam from the discharge lamp was reflected by a spherical mirror to the chopper followed by the double grating monochromator. A light beam was chopped with a frequency 5-20Hz and the monochromator limited photons energy from 0,91eV to 1,9eV. Behind the monochromator output was second harmonic filter. See **Fig. 5-4** for full spectrum obtained with the monochromator and SH filter. We were able to change intensity of the beam falling on the sample, in the range $0\text{-}10^{13}$photons/cm^{2}s by changing the interstice of the monochromator. In the **Fig. 5-5** calibration of dependence of intensity on interstice setting can be seen. Behind the SH filter was the beam finally lead to the cryostat through the glass window. Vacuum in the cryostat was in the first phase pumped with a rotary pump and in the second step by the turbopump. The closed-cycle He cryostat cooled with water, was used for measurement in the range of 10-300K. The main measurements were performed at 10K and 300K.
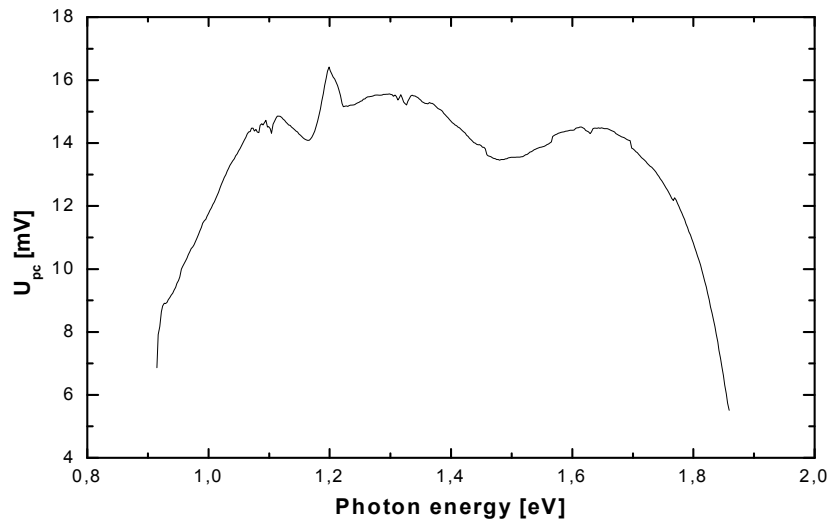
Fig. 5-4
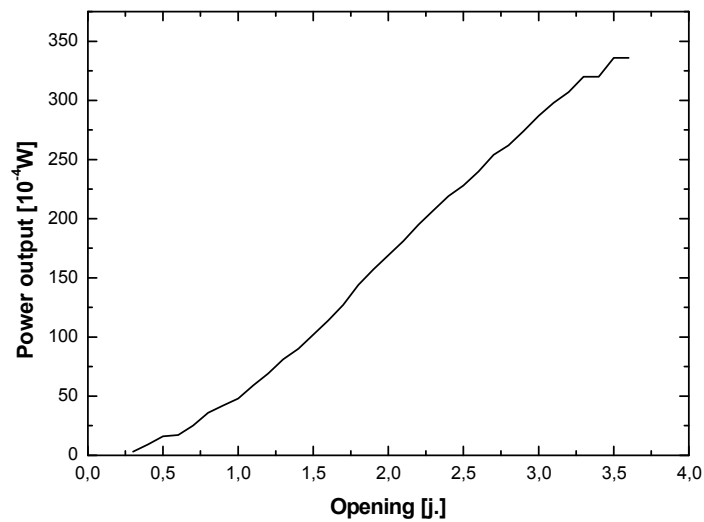*Spectrum of the discharge lamp and the SH filter, with maximum opening*

Fig. 5-5
Dependence of the beam intensity on interstice setting

    The beam spot was approximately $2mm^2$. The Keithley voltage source range we can use was 0 to 100V that corresponds to the electric field approx. $\pm(40\text{-}800V.cm^{-1})$ in the sample. The photovoltage values on the sample were received by the Lock-In amplifier and then read manually or by computer from the Keithley multimeter. The constant value of voltage on the sample was monitored by Keithley electrometer. The geometry of experiment is shown in **Fig. 5-6**. With this setup photoconductivity spectra and Lux-Ampere characteristics measurement for weak intensity of illumination were performed.
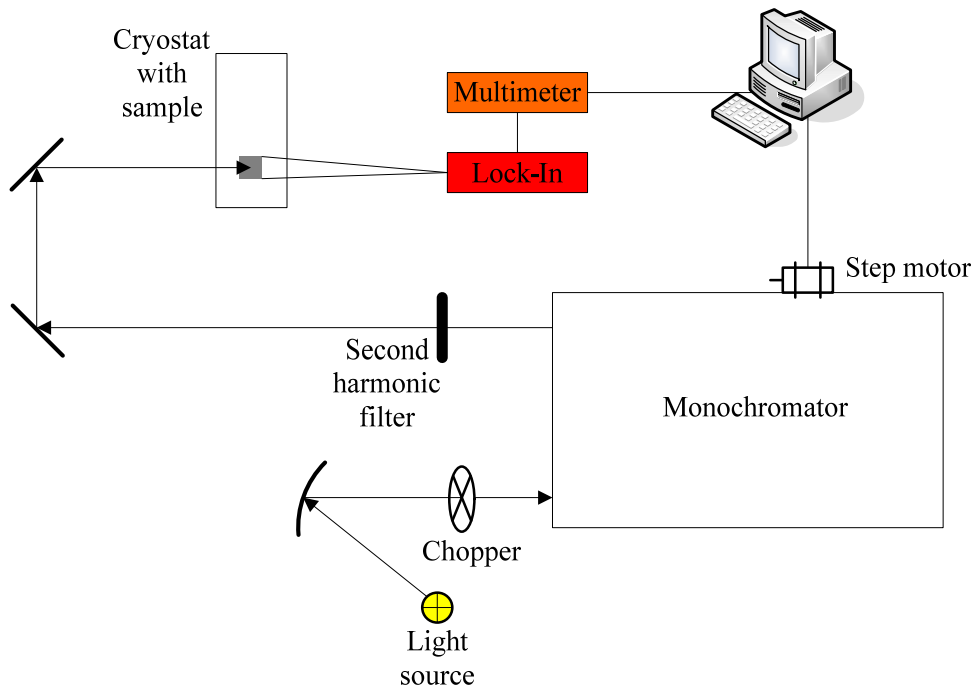
Fig. 5-6
The setup with monochromator for PL, PC and Lx-A measurements

During our measurement we always read photovoltage U_{PC} on the sample with Lock-In amplifier. To compute photocurrent values the following equation was used.

$$I_{PC} = U_{PC} \frac{(R_c + R_0)(R_C - R_0 - \Delta R)}{S.R_C.R_0(R_0 - \Delta R)} , \qquad (36)$$

Where R_0 is resistance of the sample in the dark and ΔR is change of sample resistance after area S illumination.

5.3.1 Spectral dependences

Every measurement was performed at constant temperature, electric field and constant intensity of the light. The monochromator motor was fully controlled via the computer. Every measurement took 1hour on average. Measured data were automatically read from the Keithley multimeter by the computer and stored in the text file.

5.3.2 Lux-Ampere characteristics

These measurements were performed for room temperature and 10K. Practically we changed the intensity of the light beam in range 50-300mW, where the linear dependence on an interstice setting was observed. Voltage applied on the sample was in range 0-100V, which corresponds to maximal electric field in the sample 900V.cm^{-1}.Acquired data were manually read from the Keithley multimeter and written to notebook.

5.4 Setup with the laser

The beam from the monochromatic source of the light (λ=632,8nm, 10mW He-Ne laser) was chopped with a frequency of 5-10Hz. Intensity of the light was modified with a set of grey filters (50, 20, 10, 5, 2 and 1% transmissivity). Approx. 1% penetrated through the Au semitransparent contact and participated in creation of electron-hole pairs. The illuminated area was approx. 1mm^2. All measurements were performed at room temperature with a constant above bandgap photon energy of 1.96eV. Electric field was applied in the direction of light propagation in the range of ±(40-400V.cm^{-1}). The output photovoltage was detected by a lock-in amplifier. Reading of voltage values was manual from the Keithley multimeter.
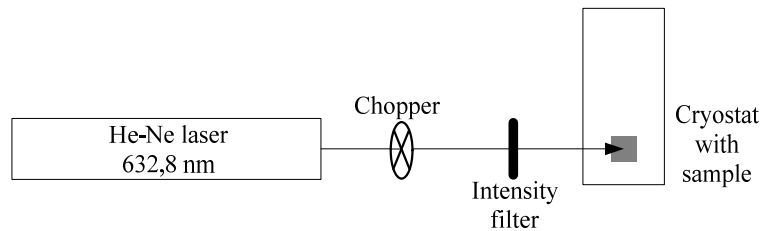

Fig. 5-7
Setup with He-Ne laser for Lx-A and V-A measurements

With this setup photoconductivity and Lux-Ampere measurements with intensity in the range 10^{14}-10^{18} photons/cm^{2}s were done.

5.5 Setup for PICTS measurement:

The PICTS (Photo-induced current transient spectroscopy) measurements were performed during my stay at Albert-Ludwigs-University in Freiburg. The apparatus consisted of a cryostat with a LED laser diode emitting light at 830nm, an amplifier and a computer for measurement control. The cryostat was cooled with liquid nitrogen. The maximum temperature range we could use for the PICTS measurement was from 77K to 350K. The sandwich configuration can be used for analyzing the transient signal under positive and negative polarities. Practically the metallic contact can be an ohmic or a blocking Schottky type. We used ohmic type of contacts, because it

was difficult to make Schottky type of contacts on high resistivity material. Schottky type would be preferable for the advantage that PICTS measurement gives better results than in case of injecting contacts. This is due to the fact that in blocking contacts the baseline for the transient is low hence the ratio signal/noise is high. The applied electric field in sample at sandwich orientation was 140V.cm^{-1}. The sample with semitransparent Au contact was pressed down to copper part of cryostat functioning as well as bottom contact and fixed with liquid silver. Light from the LED diode was flashing near Au contacts with spot approximately 1mm^2.
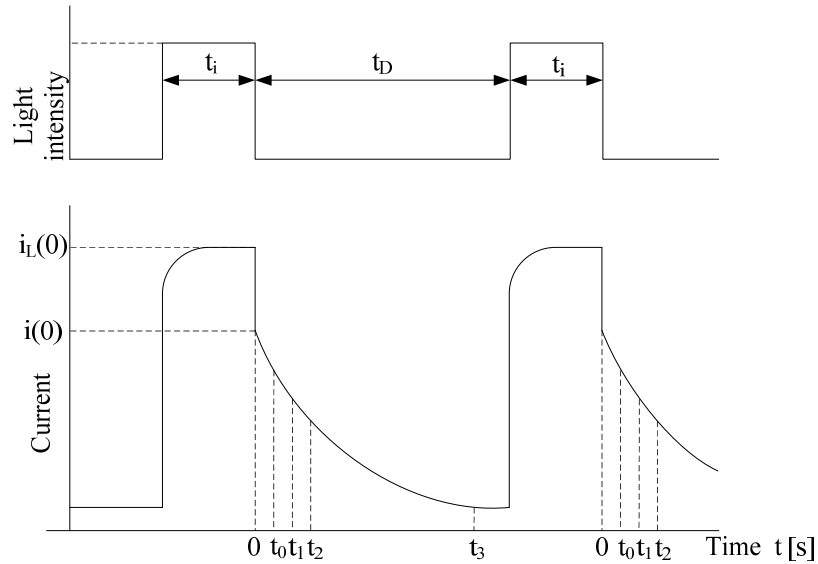
Fig. 5-8
Light and current behavior in PICTS experiment [57.]

The transient signals during the dark interval were captured at each temperature so that one whole experiment could be realized in a single temperature scan and the transients' data were stored in the texts file. One measurement with resolution 0,5K takes approximately one hour.
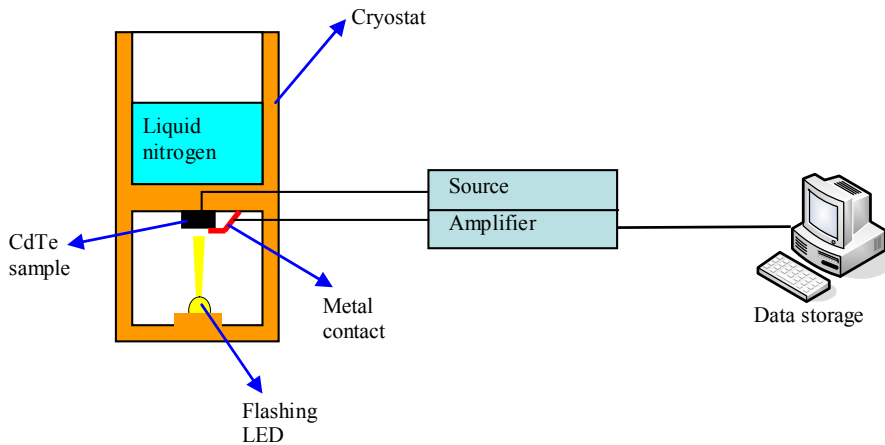

Fig. 5-9
Scheme of PICTS apparatus with cryostat cross-section

5.6 Studied samples

The high resistivity CdTe crystals investigated in this work were prepared by vertical gradient freeze method and by growth from Te solvent. One high resistivity undoped CdTe and various doped (Cl, Sn, and Ge) samples were study in this work.

Table V – Studied samples overview

Sample ref.	Dopant	Thickness [mm]	ρ [Ω.cm] 300K	Studied methods	Color in graphs
Nr.1	Cl	1.32	4×10^8	PICTS, Lx-A, Spectra	Red
Nr.2	Cl	1.48	7×10^8	PICTS, Spectra	Green
Nr.3	Sn	1.6	2×10^9	Spectra	Blue
Nr.4	Sn	1.6	8×10^8	Spectra	Cyan
Nr.5	Undoped	1.25	3×10^8	PICTS, Lx-A, Spectra	Magenta
Nr.6	Ge	1.1	5×10^8	PICTS, Spectra	Yellow
Nr.7	Sn	1.24	1×10^9	Lx-A	Dark Yellow

In this work I will maintain color schema of the samples in graphs.

6 Results and Discussion

6.1 Results of the PICTS processing

We studied several samples with the PICTS method. In this part we will discuss samples Nr. 1, 2, 5 and 6. PICTS results. The operating temperature range of the PICTS setup was from 77K up to 350K. Practically we didn't start heating from the lowest reachable temperature, because it was timely demanding to reach it and only very shallow levels should be revealed in the temperature range 77-100K. In subsequent figures sample decay transients obtained during our measurement are shown.
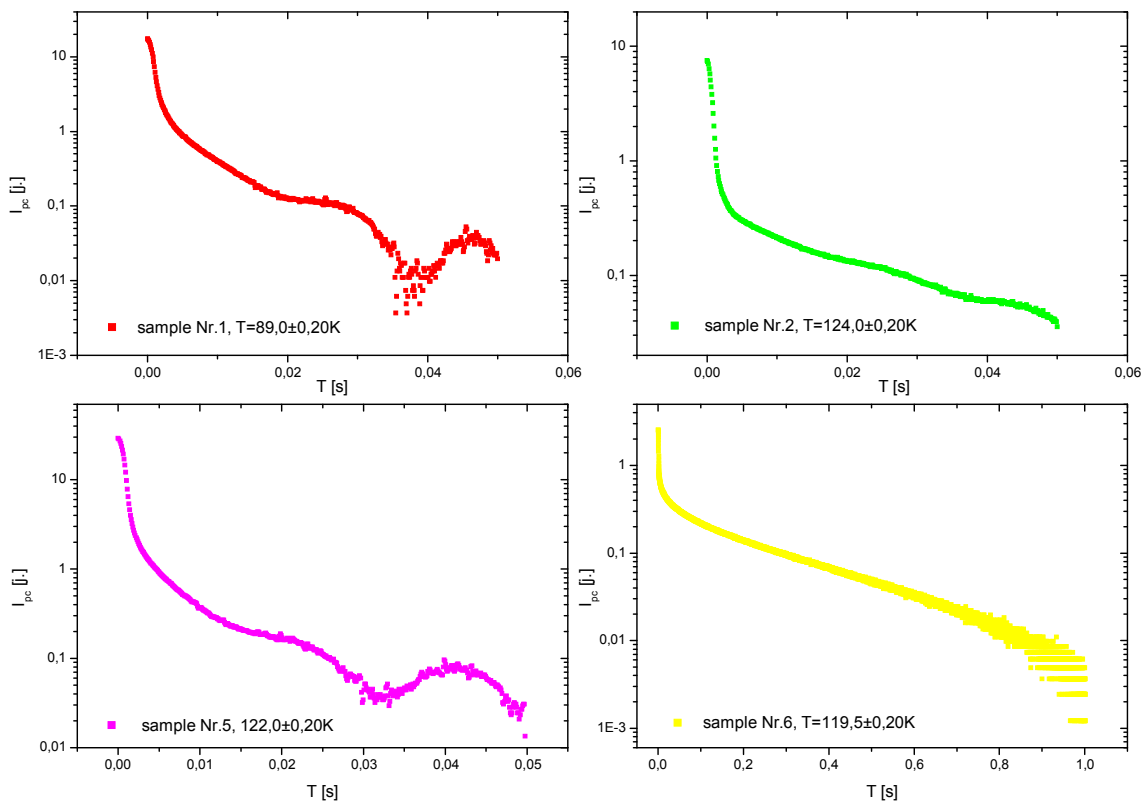
Fig. 6-1
Decay transients for selected samples

In final part of transients one can observe perturbative effects like noise or frequency of the electric network in samples Nr. 1 and 5. This is probably due to the bad electronic shield. And finally it limited us in gathering data from transients.

In **Table VI** real temperature ranges for which we studied the samples are shown. In fact measurements on each sample were done more times and finally I chose the best one. In **Table VI** marginal values of the transients´ processing interval t_0 and t_3 are presented, too.

Table VI – Measuring temperature range for the samples (1, 2, 5, and 6) and optional parameters for decay transients processing.

Sample	Temperature range [K]	t_0 [ms]	t_3 [ms]
Nr.1	89 – 299	0.4	100
Nr.2	124 -325	0.4	50
Nr.5	122 – 350	0.4	7
Nr.6	119 – 218.5	0.4	1000
	219 – 293	0.4	140

For processing of decay transients I programmed software based on MS Excel and Visual Basic for Applications, see GUI (graphics user interface) in **Fig. 6-2** and **Fig. 6-2**. I get set of spectra (approx. 100) after processing of the transients with parameters above, from which it was necessary to get values of temperatures T_m of the spectra peaks. In **Fig. 6-4** sample spectrum with marked peaks we considered for further processing is shown. The positions of peaks´ maxima were found by the script written by Doc. RNDr. Jiří Bok, CSc.
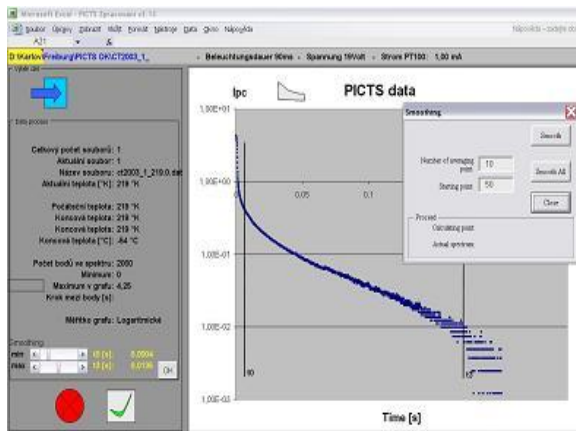
| **Fig. 6-2** | **Fig. 6-3** |

Fig. **6-2** *show the GUI of program for decay transients processing*
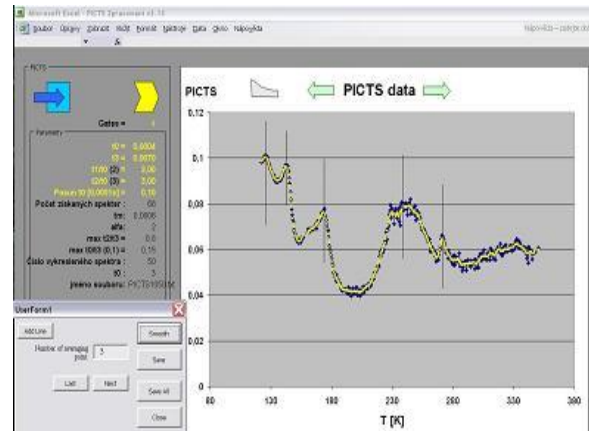*Fig.* **6-2** *show the GUI of program for PICTS spectra overview and smoothing*

In **Fig. 6-4** set of normalized spectra, where the movement of the peaks can be perceived, is presented.
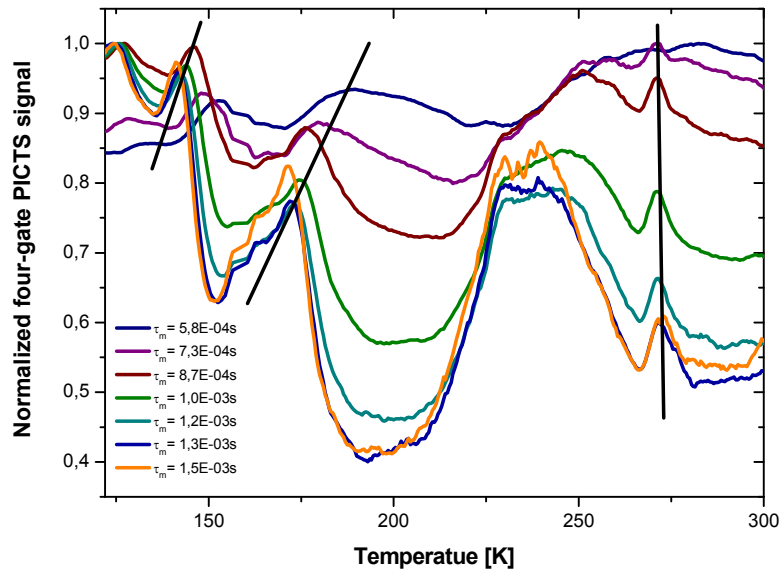

Fig. 6-4
Set of normalized PICTS spectra for the sample Nr.5.

The final part of the data processing, the Arrhenius diagram linear apparent fit and computing of activation energies and capture cross-sections, was prepared in Origin software from OriginLab Corporation. In following figures relevant Arrhenius diagrams are shown.
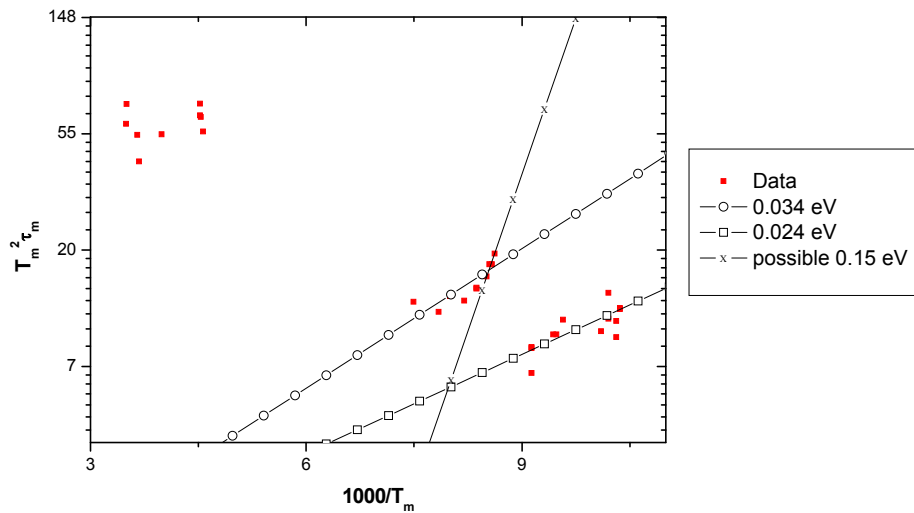

Fig. 6-5
Sample Nr.1 (S81) Arrhenius diagram with apparent fits of observed levels

Just two shallow levels were found in sample Nr.1. Another deep level will be probably present, but due to insufficient measured temperature range we are not able to interlay apparent line through the data in Arrhenius diagram (see the cluster of points at $1/T_m \sim 4$).
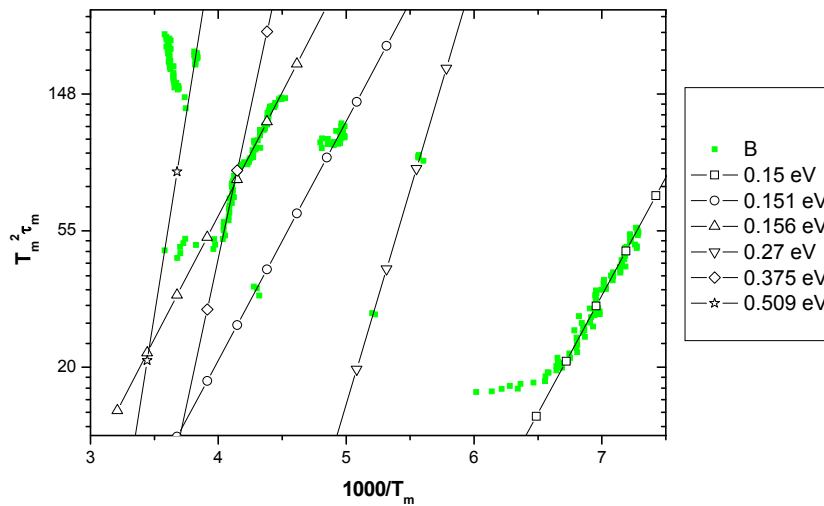

Fig. 6-6
Sample Nr.2 (D38) Arrhenius diagram with apparent fits of observed levels

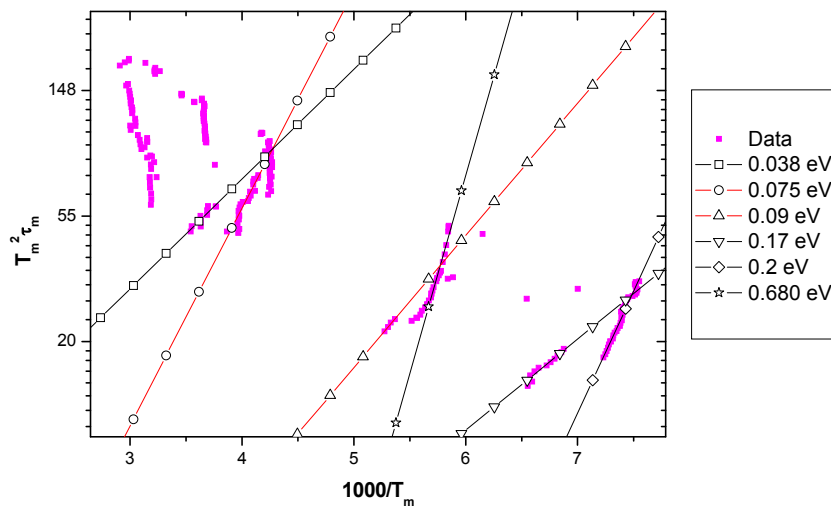Six discrete levels were found, the deepest level has ionization energy 0.509eV

Fig. 6-7
Sample Nr.5 (BG7) Arrhenius diagram with apparent fits of observed levels

In sample Nr.5 we have found 6 levels, the deepest level has ionization energy 0.68eV.
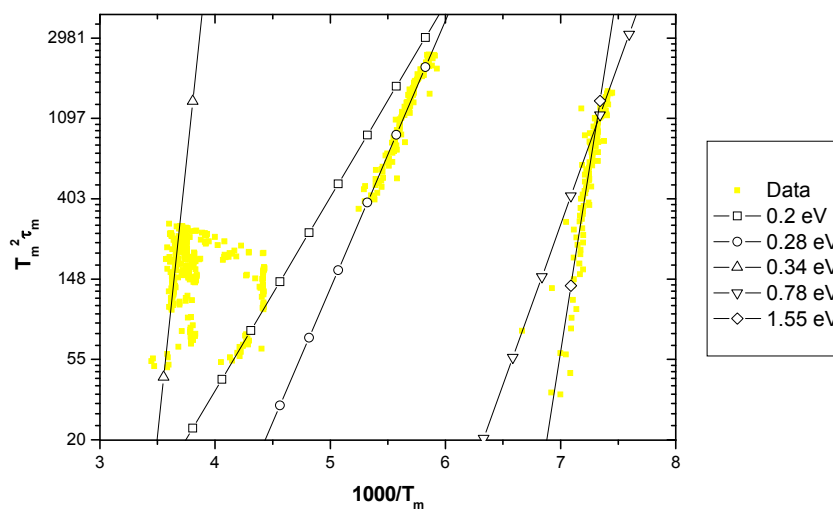
Fig. 6-8
Sample Nr.6 (CT2003) Arrhenius diagram with apparent fits of observed levels

In sample Nr.5 six discrete levels were found, the deepest level has ionization energy 0.78eV. We have not found any shallow levels in this sample.

Near midgap level in Ge doped sample Nr.6 (0.78eV) was observed. This is good agreement with data in the literature [32.]. This level is usually ascribed to Ge_{Cd}. Cl doped samples gave a mixed results. No deep level could be found in sample Nr.1, while in sample Nr.2 a deep level 0.5eV was observed. Nominally undoped sample Nr.5 a deep level of unknown origin with a high capture cross-section ($\sim 10^{-11} cm^2$) can be seen.

Summary of results of PICTS measurements is presented in Table VII.

Table VII – Summary of results of PICTS measurement and analysis

Sample	Energy [eV]	Capture cross-section for electrons [cm^2]	Capture cross-section for holes [cm^2]
Nr.1	0.024	9.3 x 10^{-22}	1,2 X 10^{-22}
	0.034	1.1 X 10^{-21}	1.3 x 10^{-26}
Nr.2	0.15	3.1 x 10^{-18}	3.8 x 10^{-19}
	0.151	3.1 x 10^{-20}	3.8 x 10^{-21}
	0.156	1.4 x 10^{-20}	1.7 x 10^{-21}
	0.375	4.8 x 10^{-16}	6 x 10^{-17}
	0.501	2.4 x 10^{-12}	2.4 x 10^{-13}
Nr.5	0.038	3.7 x 10^{-19}	4.7 x 10^{-20}
	0.075	2.7 x 10^{-22}	3.4 x 10-^{24}
	0.09	7.1 x 10^{-21}	8.9 x 10^{-22}
	0.17	1.2 x 10^{-18}	1.5 x 10^{-19}
	0.19	3.7 x 10^{-19}	4.7 x 10^{-20}
	0.68	1.4 x 10^{-10}	1.7 x 10^{-11}
Nr.6	0.20	2.4 x 10^{-19}	3.1 x 10^{-20}
	0.28	7.9 x 10^{-17}	9.9 x 10^{-18}
	0.34	2.6 x 10^{-12}	3.3 x 10^{-13}
	0.78	5.7 x 10^{-10}	7.1 x 10^{-11}

We conclude, that several energy levels were revealed by PICTS method in all investigated samples. Deep levels, which can effectively pin the Fermi level near the midgap were observed in samples No.2, 5 and 6. In sample No.1 no deep level was found. The reason can be, that near midgap energy levels with smaller capture cross sections emit carriers at higher temperatures (>300K). Here the signal can be smaller than dark current. Another reason can be that the concentration of the level is smaller and the signal is below the sensitivity limit of the setup.

PICTS method can be considered as a useful one in deep levels investigation, but it does not necessarily provide full information about their presence. It also does not reveal the type of the trap and its concentration. Therefore additional investigations had to be done. In order to identify possible presence of deep levels even in samples, where they are not found by spectroscopic methods (PICTS, TEES) and to estimate their maximum concentrations, measurements of lux-ampere characteristics and photoconductivity spectra in dependence of the applied external electric field were performed.

6.2 Lux-Ampere characteristics

6.2.1 Acquired data – basic characteristics

Measurements were performed on samples Nr.1, 5 and 7, for 10K and room temperature, and for electric fields 40 and 400V.cm^{-1} in both polarities.

6.2.1.1 Room temperature measurements – 300K

In the following figures obtained characteristics of photocurrent densities in dependence of photon flux for three high resistivity CdTe samples are shown. Parameter α represents the slope of the dependence.
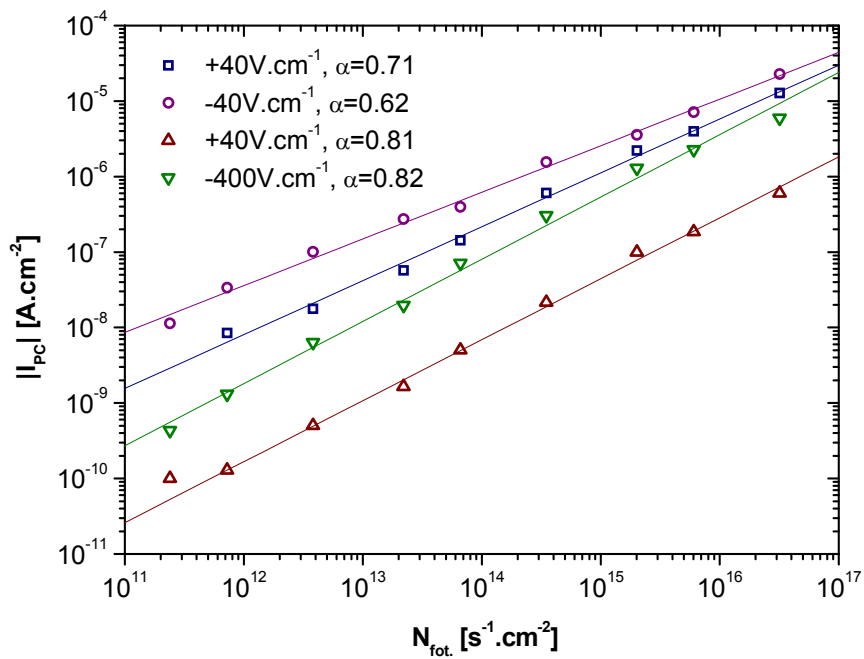

Fig. 6-9
Room temperature Lx-A characteristic of sample Nr.1
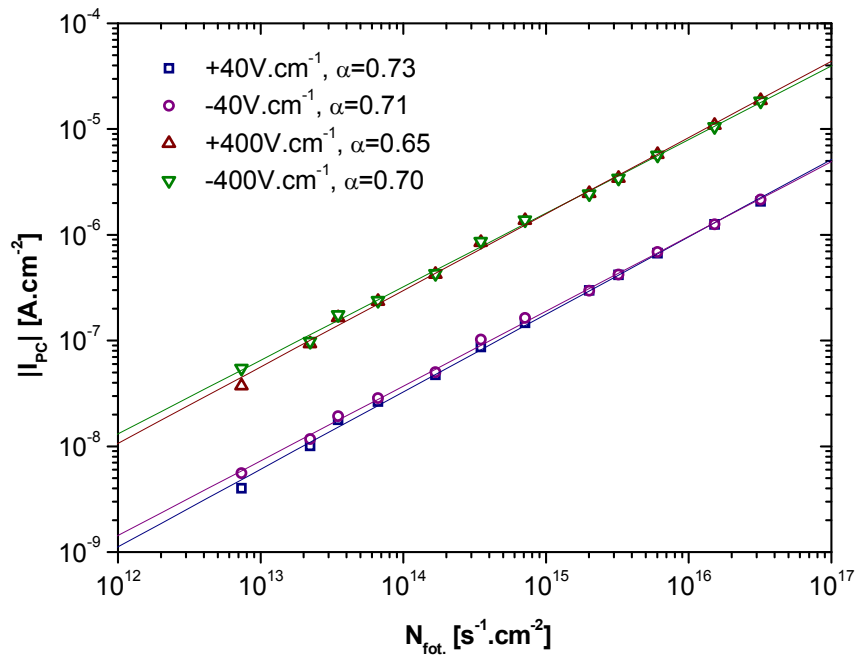
Fig. 6-10
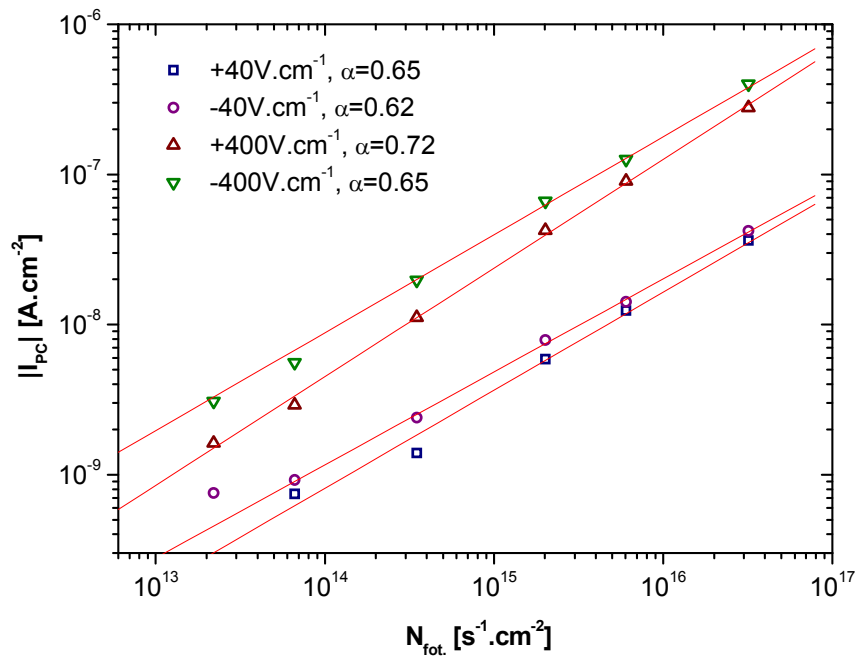*Room temperature Lx-A characteristic of sample Nr.5*

Fig. 6-11
Room temperature Lx-A characteristic of sample Nr.7

Summary of Lx-A characteristics for all 3 samples and four applied electric fields is shown in the following figure.
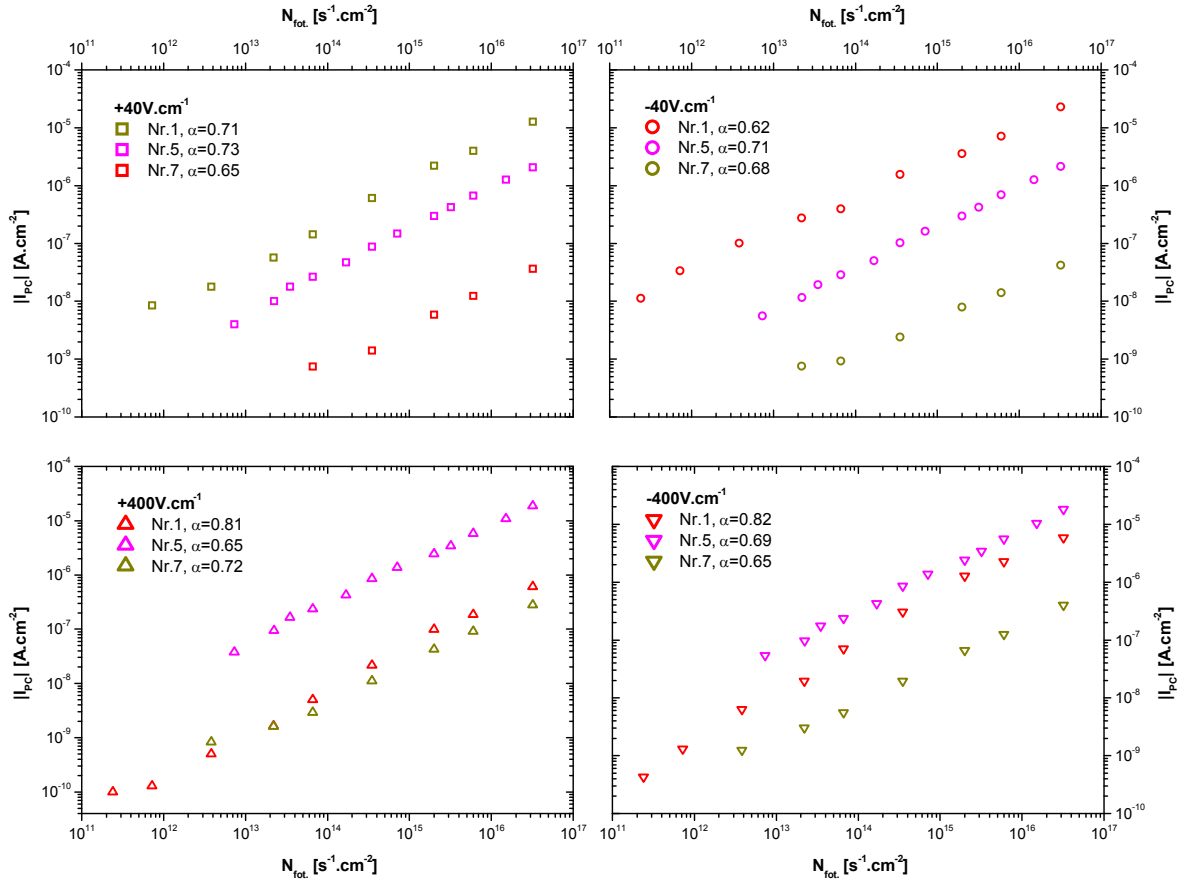

Fig. 6-12

Room temperature Lx-A characteristics of samples Nr.1, 5, and 7 measured at electric field $\pm 40V.cm^{-1}$, $\pm 400V.cm^{-1}$

Exact values of the slopes are summarized in **Table VIII**. All room temperature lux-ampere characteristics have slope in range 0.62-0.82 for used beam intensities. It is apparent that all that characteristics' slopes are similar in variously doped samples and for applied fields. This gives us a clue that sublinear dependences of Lx-A characteristics at room temperature are due to a general phenomenon. Nevertheless, differences among samples doped by various dopants can be seen. The smallest slope at $\pm 400V/cm$ was found in Cl doped sample Nr.1.

Table VIII – Slopes of lux-ampere characteristics for room temperature

Sample	α $E = 40V.cm^{-1}$	α $E = -40V.cm^{-1}$	α $E = 400V.cm^{-1}$	α $E = -400V.cm^{-1}$
Nr.1	0,71	0,62	0,81	0,82
Nr.5	0,73	0,71	0,65	0,70
Nr.7	0,65	0,62	0,72	0,65

6.2.1.2 Low temperature measurements – 10K

As a complementary technique we performed measurement for low temperature 10K. Overlinear Lux-Ampere characteristics with slope $\alpha>1$ were obtained in some cases and it does corresponds with literature [58.]. A detailed study of that effect is not the aim of this work.
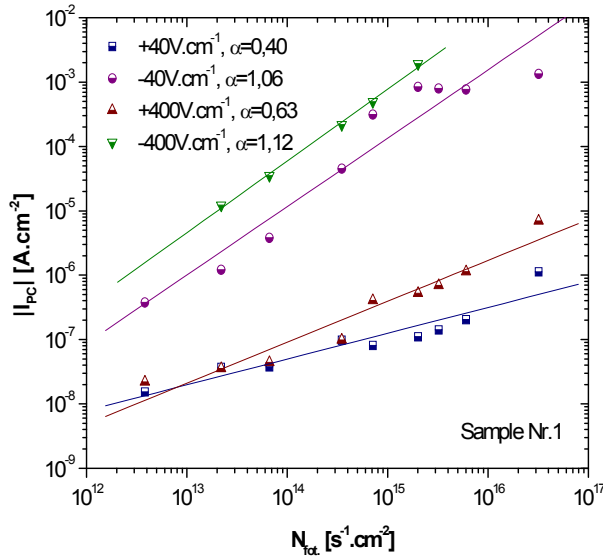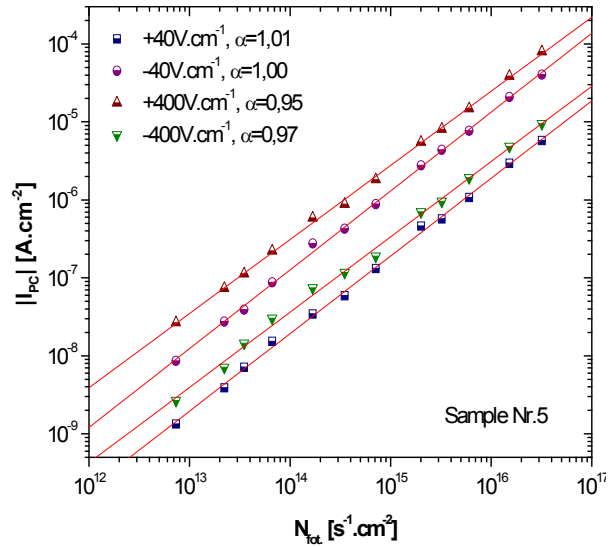

Fig. 6-13
Lx-A characteristic of sample Nr.1 for 10K

Fig. 6-14
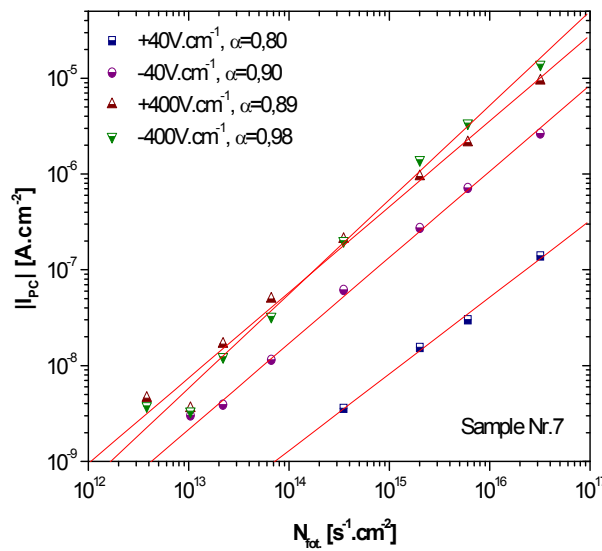*Lx-A characteristic of sample Nr.5 for 10K*

Fig. 6-15
10K Lx-A characteristic of sample Nr.1 with apparent fits

Summary of obtained characteristics is shown in the following table

Table IX – Slopes of lux-ampere characteristics for 10K

Sample	α E = 40V.cm^{-1}	α E = -40V.cm^{-1}	α E = 400V.cm^{-1}	α E = -400V.cm^{-1}
Nr.1	0,4	1,06	0,63	1,12
Nr.5	1,01	1	0,95	0,97
Nr.7	0,8	0,9	0,89	0,98

6.2.2 Model of Lux-Ampere characteristics

Due to the fact, that discrete levels were observed by PICTS measurements, the model of screening of electric field by space charge [36.] was taken as a base for theoretical evaluation of Lx-A characteristics. Only room temperature data and positive electric field (transport of electrons through the sample to the back electrode) were modeled.

The numerical solution was calculated by the software programmed by Doc. Roman Grill, CSc. Evaluation of PICTS measurements could be finished only recently. Therefore modeling of Lx-A characteristics was done for energy levels known from literature. Variation of modeling parameters (like S_e, S_n) will be discussed in order to draw conclusions for a wide range of energy levels in high resistivity CdTe. A very detailed analysis of midgap levels in CdTe including capture cross-sections of both electrons and holes was performed in Ref.[6]. Therefore these values ($E_{deep}=E_c-0.7eV$, $\sigma_e=4.5\times10^{-16}cm^2$, $\sigma_h=2.9\times10^{-14}cm^2$) were taken to start numerical simulations. Results are shown in **Fig. 6-16**. The slope of Lx-A characteristic for the concentrations of the midgap level from $N_{deep}\leq1.10^{12}cm^{-3}$ to $N_{deep}=7.10^{12}cm^{-3}$ decreases from 1 to 0.53. Full squares represent the result for $N_{deep}=7.10^{12}cm^{-3}$ and without calculation of the Poisson equation, it means without influence of space charge on the transport.
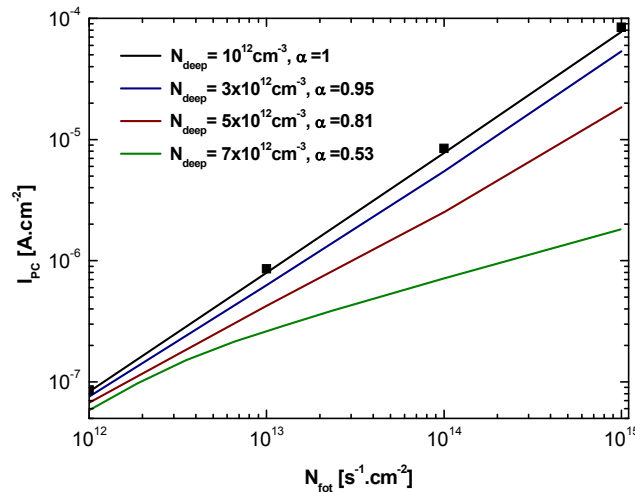

Fig. 6-16

Numerical solution of Lx-A characteristics for
$N_{deep}=1-7.10^{12}cm^{-3}$, $E_{deep}=E_C-0.7eV$, $\sigma_e=4.5\times10^{-16}cm^2$, $\sigma_e=2.9\times10^{-14}cm^2$

From results of this simulation we can claim that the main (significant) influence on sublinear dependences of Lx-A has space charge, which is accumulated on the deep level.

For simulation of the sample we apply negative charge on the front contact and positive charge on the back contact, so that electrons are attracted through the whole sample volume to backside contact. Distribution of space charge in the sample for three different photon fluxes is shown in **Fig. 6-17**. In a thin front layer below the front illuminated contact positive charge is accumulated due to capturing of photogenerated holes on deep level, which has a higher capture cross section for holes than for electrons. The main part of the sample volume is negatively charged. Electrons drift in electric field to backside contact and are captured by the deep levels. These captured electrons form a space charge and screen the electric field from the backside positive contact. Electrons are attracted to the back contact by a substantially lower field, than in case of electric field +400V.cm^{-1}. Electron-hole recombination in the area adjacent to the front contact will be augmented due to a lower electron's mid-drift velocity. As a result we can observe characteristic sublinear lux-ampere characteristics. Simulation of development of electric field in sample volume can be seen in **Fig. 6-18**. Electrons in the front thin layer are moved only by diffusion mechanism right to depth approx 0,02cm and then they are accelerated by the applied electric field.
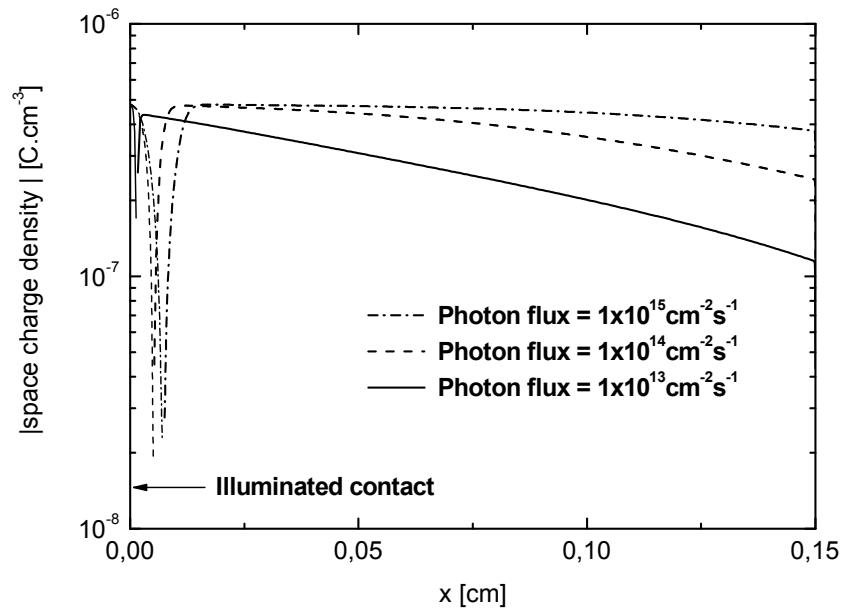

Fig. 6-17

Development of space charge density through the sample for assumed parameters
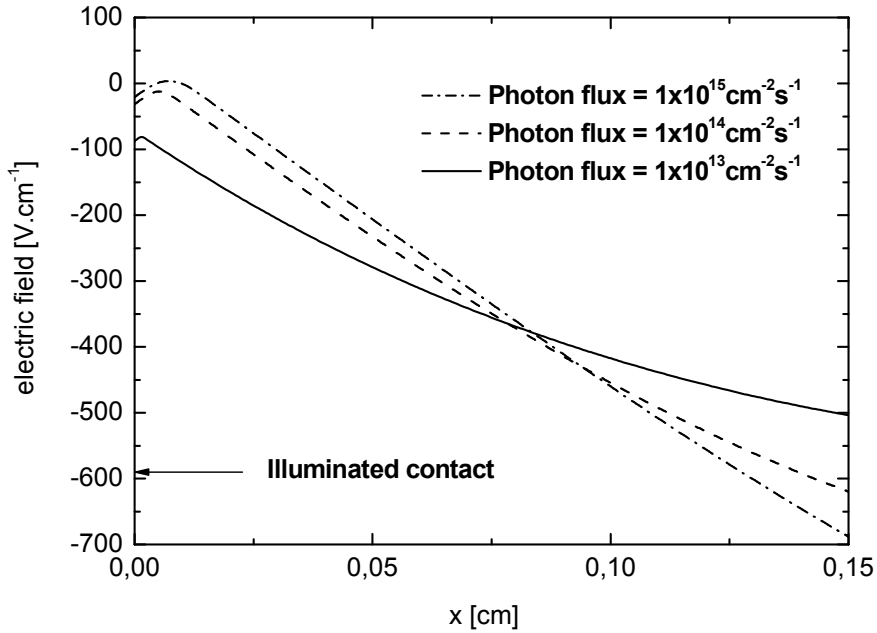
Fig. 6-18
Effective electric field in the sample for assumed parameters

We were interested in influence of cross sections of electrons and holes on the observed effects, since they vary for a wide range of dopants and samples' purity. Simulation for different cross section of electrons and holes is shown in **Fig. 6-19** and **Fig. 6-20**. As you can see space charge in the sample is not significantly affected by capture cross sections.
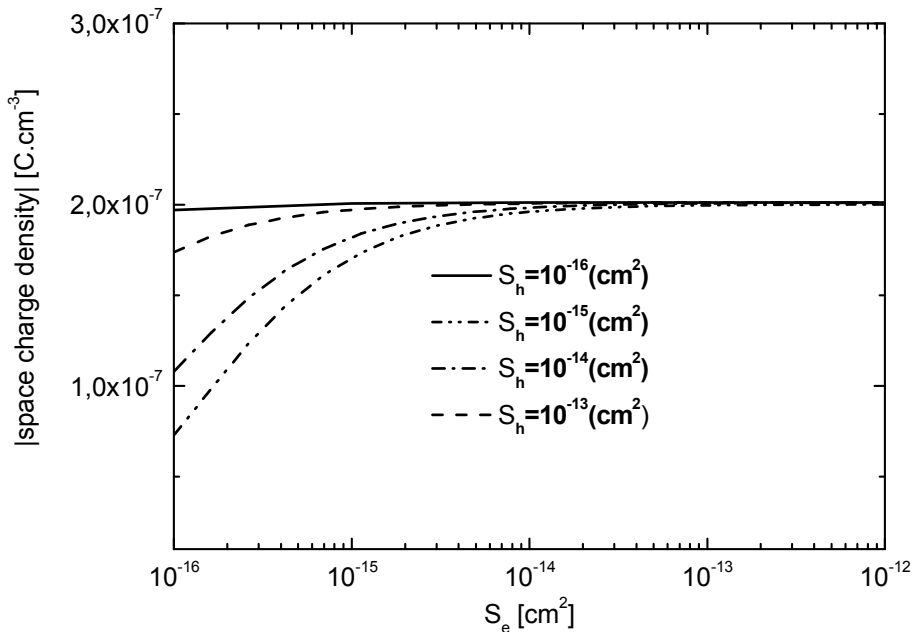

Fig. 6-19
Space charge density in sample volume for various cross sections of holes
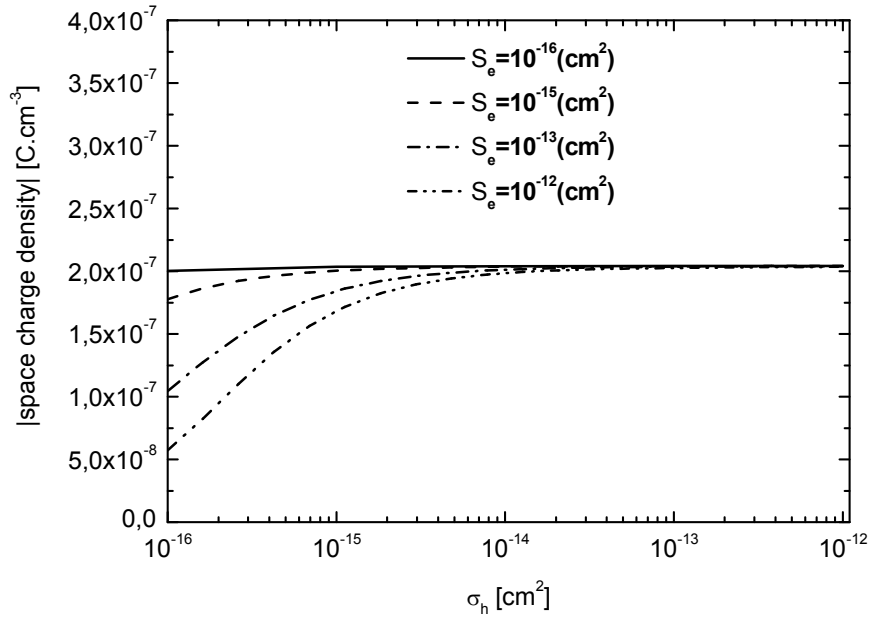
Fig. 6-20

Space charge density in sample volume for various cross sections of electrons

This result can be explained as follows. Space charge of electrons on deep levels can be removed by recombination of electron with hole captured on this level. This process is nevertheless limited by presence of holes in the sample volume. In high resistivity samples the concentration of thermal holes is small and photogenerated holes are localized mainly in the front thin layer. Electrons on center can therefore recombine only with holes drifting from backside contact to the front negative contact through the whole sample. Sum of thermally generated holes and holes generated by drawing off electrons by the positive contact is substantially lower than number of photon-and thermally generated electrons in case of photon densities used in the experiment. And thus recombination process of captured electrons and holes is small and the space charge is basically independent of electrons´ and holes´ cross sections [59.].

We therefore summarize, that the concentration $N_{deep}<10^{13}cm^{-3}$ can be estimated for slopes of lux-ampere characteristics $\alpha>0.5$ of high resistivity CdTe. This result strongly supports the models assuming the formation of a high resistivity state with a minimum deep level doping.

Comparison of the simple two-layers model [36.] with our detailed numerical calculation of the screening model was accomplished. In case of photon flux $1x10^{14}$ $s^{-1}cm^{-2}$, the maximum concentration of deep levels $N_{deep}=5x10^{11}$ is estimated to reach sublinear dependences in simple model. Our precise numerical simulation for the same parameters shows no measurable deviation of Lx-A characteristics up to approx. $N_{deep}=3x10^{12}$.

6.3 Basic characteristic of photoelectric transport – spectral dependences

We undertook spectral resolution measurement to get insight in basic material characteristics. Applied electric fields and photon energy range are shown in **Table X**. We worked with resolution 2meV. As the result we get set of spectra for room and low (10K) temperature.

Table X – Basic conditions for spectral resolution measurements

Sample	Temperature [K]	Energy [eV]	El. Field (+) [V.cm^{-1}]	El. Field (-) [V.cm^{-1}]
Nr.1	300	1.36 -1.65	25, 212, 460, 600	30, 135, 225, 320, 460, 600
	10	1.42 -1.71	32, 130, 190	0.6, 32, 320, 570
Nr.2	300	1.32 – 1.65	135, 340	135, 340
	10	1.43 – 1.72		35, 68, 135, 340
Nr.3	300	1.36 -1.69	32, 65, 130, 320	32, 65, 130, 320
	10	1.36 -1.69	125, 310	125, 310
Nr.4	300	1.36 -1.69	130, 220	25, 125, 210
Nr.5	300	1.31 -1.65	80, 160, 400, 720	80, 160, 400, 720
	10	1.42 – 1.78		80, 160, 400, 720
Nr.6	10	1.36 -1.74	85, 130, 320	120, 300

6.3.1 Acquired data

Acquired spectra for various samples can be only roughly compared among them according to signal intensity, because we it was not possible to guarantee exactly same light beam intensity falling to the sample due to variation of semitransparent golden layer. Measurements were performed in both electric field polarities. In case with positive charge on backside contact and negative charge on front illuminated contact, are electrons generated at front layer drifted by the applied electric field through the whole sample volume. This is the most interesting case, because such arrangement is used for detectors. Holes are drifted to backside contact in case of inverse polarity.

6.3.1.1 Room temperature

In case of room temperature measurements we obtained classical photocurrent spectra. There were two cases of peak position behavior, in first case (**Fig. 6-21**) was observed shift of photopeak to higher energies with applied field and in second case no shift was observed (**Fig. 6-22**).
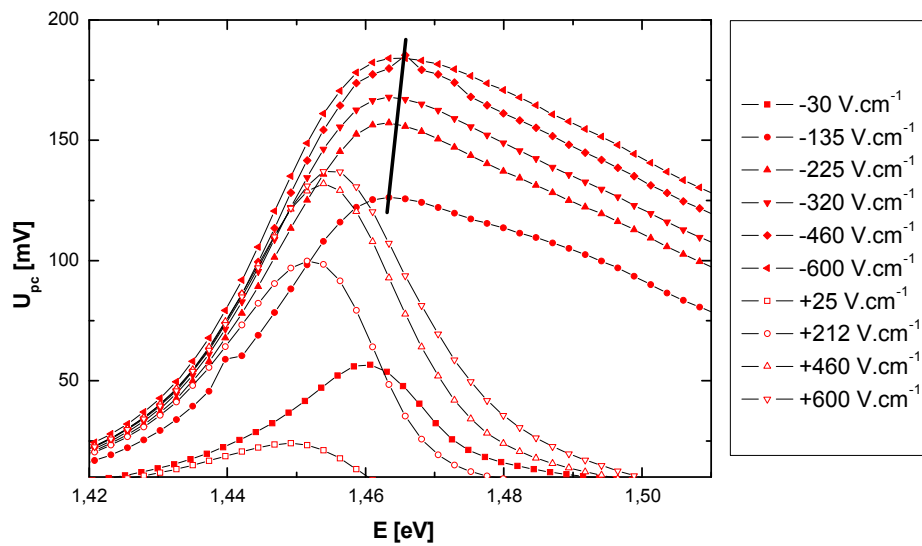
Fig. 6-21
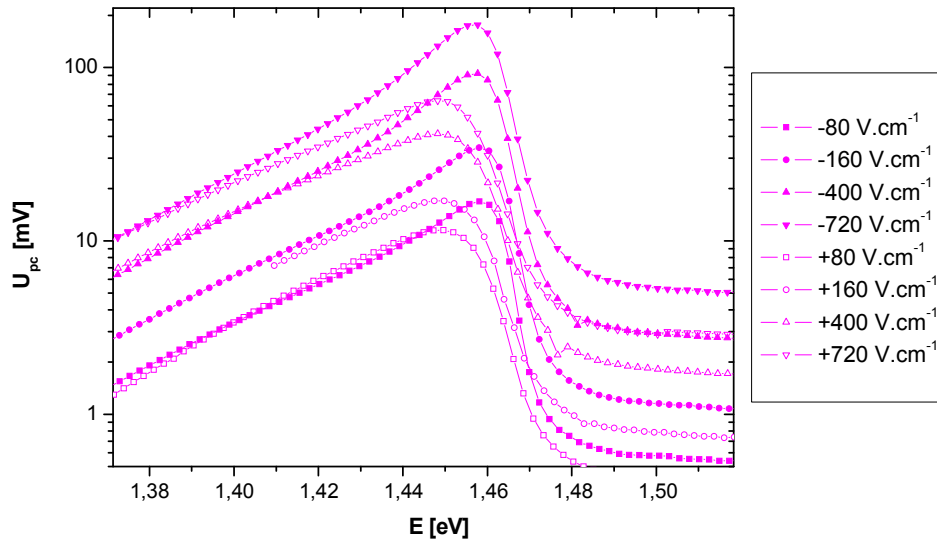*Spectral dependences of sample Nr.1 at room temperature and varied electric field*

Fig. 6-22
Spectral dependences of sample Nr.5 at room temperature and varied electrical field

6.3.1.2 Low Temperature

At 10K we obtained other typical characteristic of spectral dependences. Typical shift in **Fig. 6-23** of photopeak to lower photon energies with increasing applied electric field is shown.
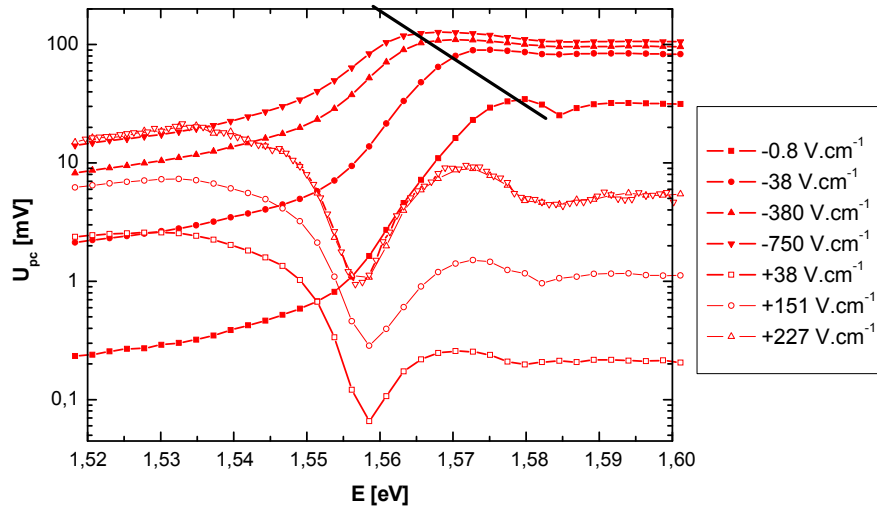

Fig. 6-23
Spectral dependences of sample Nr.1 for 10K and varied electrical field
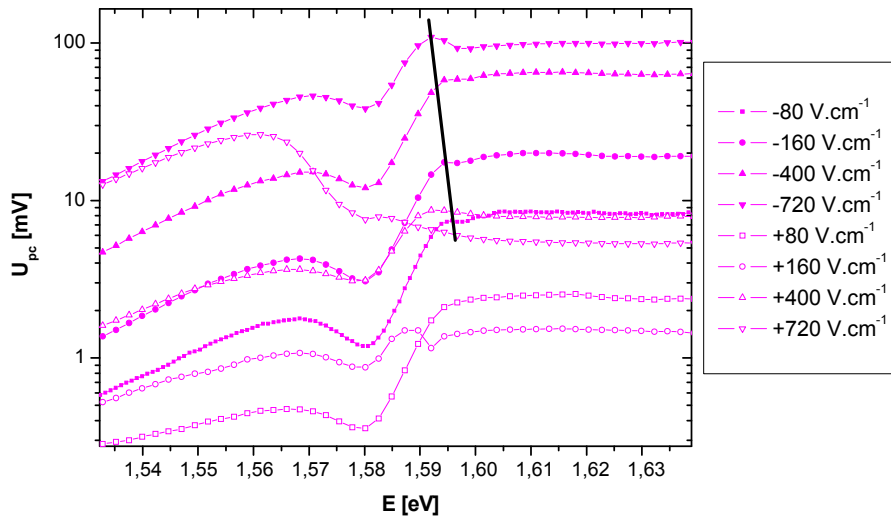

Fig. 6-24
Spectral dependences of sample Nr.5 for 10K and varied electrical field

We suppose that explanation of this phenomenon could be in inclination of band gap in applied electric field. This could lead to increasing probability of liberation of carriers from potential minima existing in the material due to various types of fluctuations to conduction band (electrons) and valence band (holes). This effect is stronger if the whole sample in irradiated it means for lower absorption coefficients. Thus shift of PC peak to lower absorption coefficients will be observed. The model of electron liberation in applied electrical field is showed in **Fig. 6-26**.
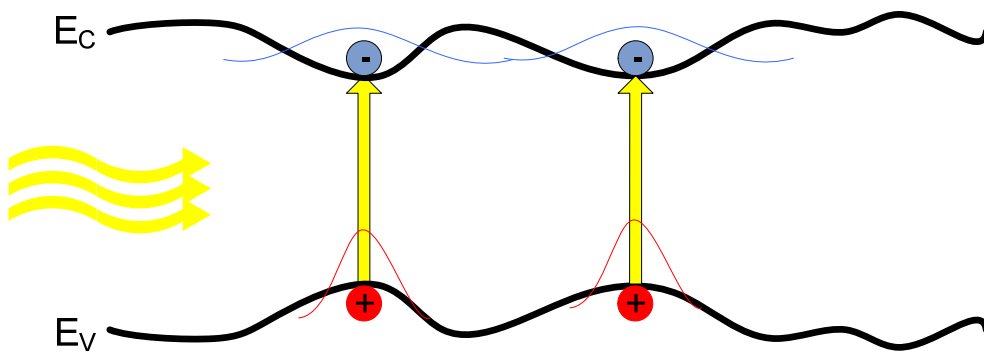

Fig. 6-25
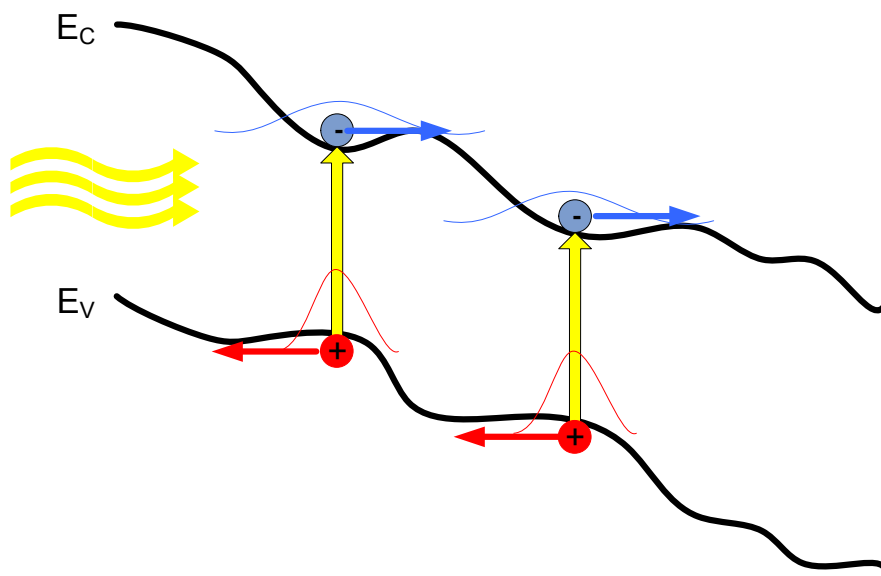*Model of bandgap without the applied electrical field*

Fig. 6-26
Liberation of localized carriers from potential minima in applied electric field model

Summary of photo-peaks position for our set of samples is shown in the following figures.

Fig. 6-27

Photo-peak position summary for our set of samples for both polarities and various applied electric field at room temperature (300K).

In our case electrons drift through the sample volume for negative electric fields, experimentally it means that backside contact is positive. There is a typical shift of photocurrent peak up to 10meV in applied electric field 500V.cm^{-1} for both polarities. The main shift is achieved in lower fields with a tendency to saturate the photopeak position in higher applied electrical fields.
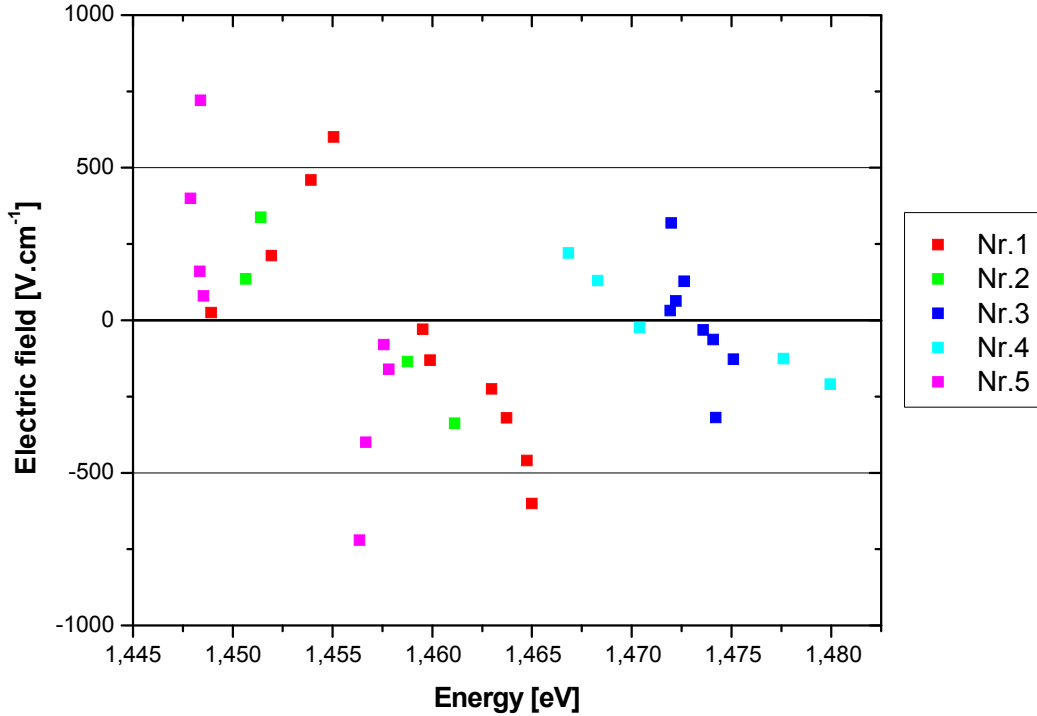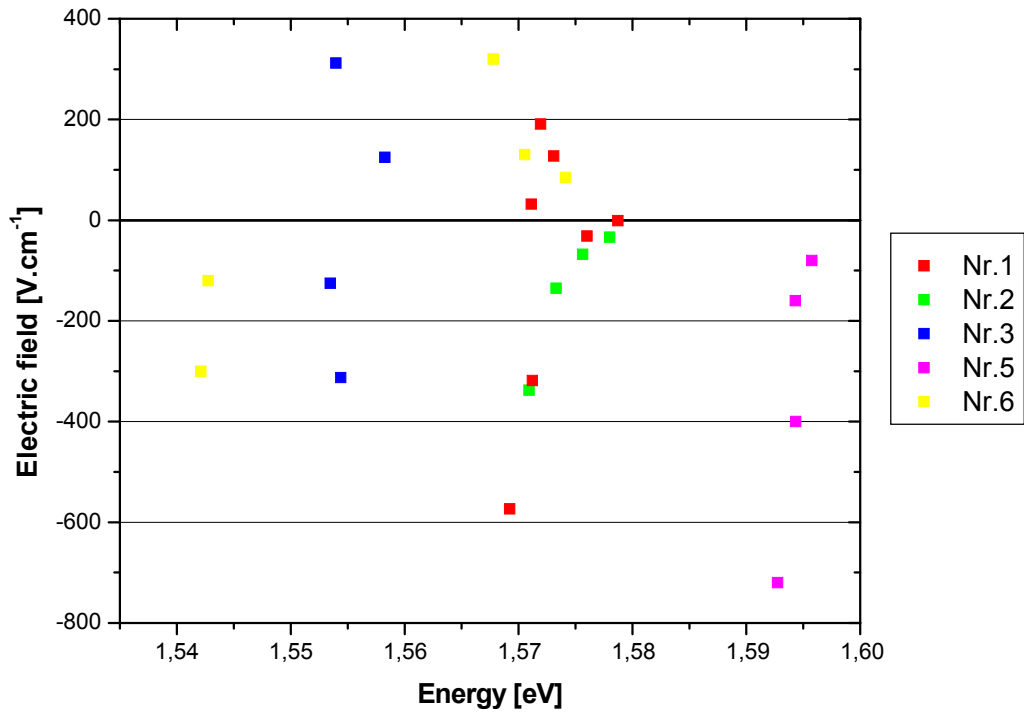
Fig. 6-28

Photo-peak position summary for our set of samples for both polarities and various applied electric field at low temperature 10K

At all samples shift of photocurrent peak to lower photon energy for higher electric fields is visible. The shift is typically 5meV in applied electric field 500V.cm^{-1} and both polarities.

6.3.2 Model of the photoelectric transport

In the following section we will focus on room temperature and on case when illuminated contact has negative charge and electrons generated in the front layer must drift through the whole sample to recombine on the backside positive contact, which is the most practically applicable arrangement. Numerical simulation of a photocurrent in the sample was performed for typical parameters of one midgap level and capture cross sections $S_n=10^{-14}cm^2$, $S_h=10^{-13}cm^{-3}$. In this work we will in detail present case of applied electric fields 250 and 400V.cm^{-1}. No reflection of passed light on back contact is assumed. Reverse configuration, which concentrates on transport of holes through the sample, can be solved by the same way.

In **Fig. 6-29** are shown results for various deep level concentrations without computing of Poisson equation, it means without influence of a space charge. It is obvious that for all level concentrations there is no photo-peak shift achieved with the change of electric field. This result does not correspond with our experimental data, where the photopeak shift with electric field is clearly visible. The photo-peak is only moved to higher absorption coefficients, which correspond to higher photon energies, and magnitude of photocurrent is decreased with increasing of the deep level concentration. It can be explained that due to a higher concentration of deep level electrons will be more captured on the traps and subsequently recombine with photogenerated holes. This causes abatement of electrons relaxation time what we can observe as a photocurrent decrease. This effect is more intense for lower absorption coefficients, where the whole sample volume is irradiated.
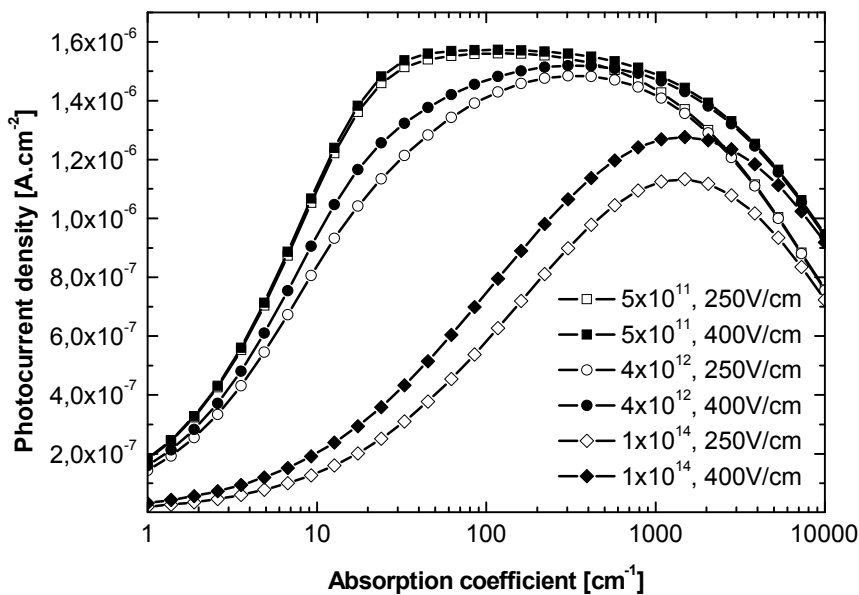

Fig. 6-29
Calculated spectral dependence of photocurrent without Poisson equation

In second case shown in **Fig. 6-30** we undertook computing with Poisson equation, it means with subsumption of space charge influence. This is a much more complicated case. We can still observe decreasing of maximal photocurrent due to higher recombination on the center for higher level concentrations. Furthermore there can be seen a shift of the photocurrent peak in applied electric field. For our parameters it is most distinct for deep level concentration 4×10^{12}cm^{-3}. Here the effect of the space charge is significant. In case of low deep level concentration 5×10^{11}cm^{-3} there is no apparent photocurrent change in comparison with sample without charge screening influence. In samples with a higher concentration of deep level we can observe high photocurrent drop due to high recombination and screening, such material would be bad detector. It is clear from our result that with higher applied electric field the relative influence of space charge screening decreases and spectra are approaching to spectra computed without Poisson equation.
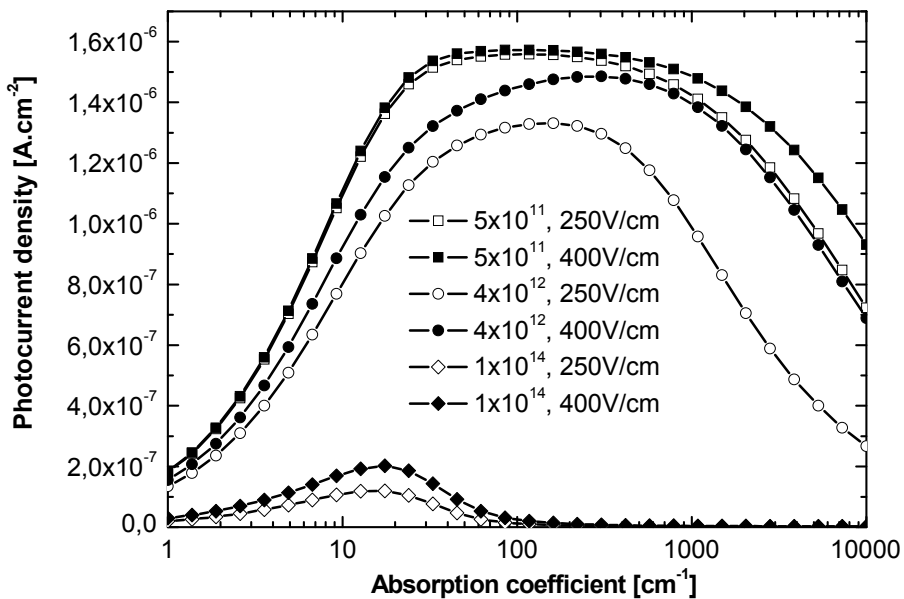

Fig. 6-30
Calculated spectral dependence of photocurrent with Poisson equation
(N_{deep}=5x10^{11}-1x10^{14}cm^{-3}, σ_e=10^{-14}cm^2, σ_h=10^{-13}cm^2, E_{deep}=E_F=0.5E_g)

Subsequently will be discussed a detailed solution for a sample with concentration of deep level 4×10^{12}cm^{-3} and absorption coefficient 5000cm^{-1} for both cases of applied electrical field 250 and 400V.cm^{-1}. In the following figure are compared developments of free electrons and holes concentrations (n, p), effective electric field (El. Field), Fermi energy of electrons and holes (Fn, Fp), space charge density (ρ), relaxation time of electrons and holes (τ_n, τ_p) and filling factor of deep level by electrons (Fill_e) in the sample volume. Zero x-axis is set at the front illuminated contact.
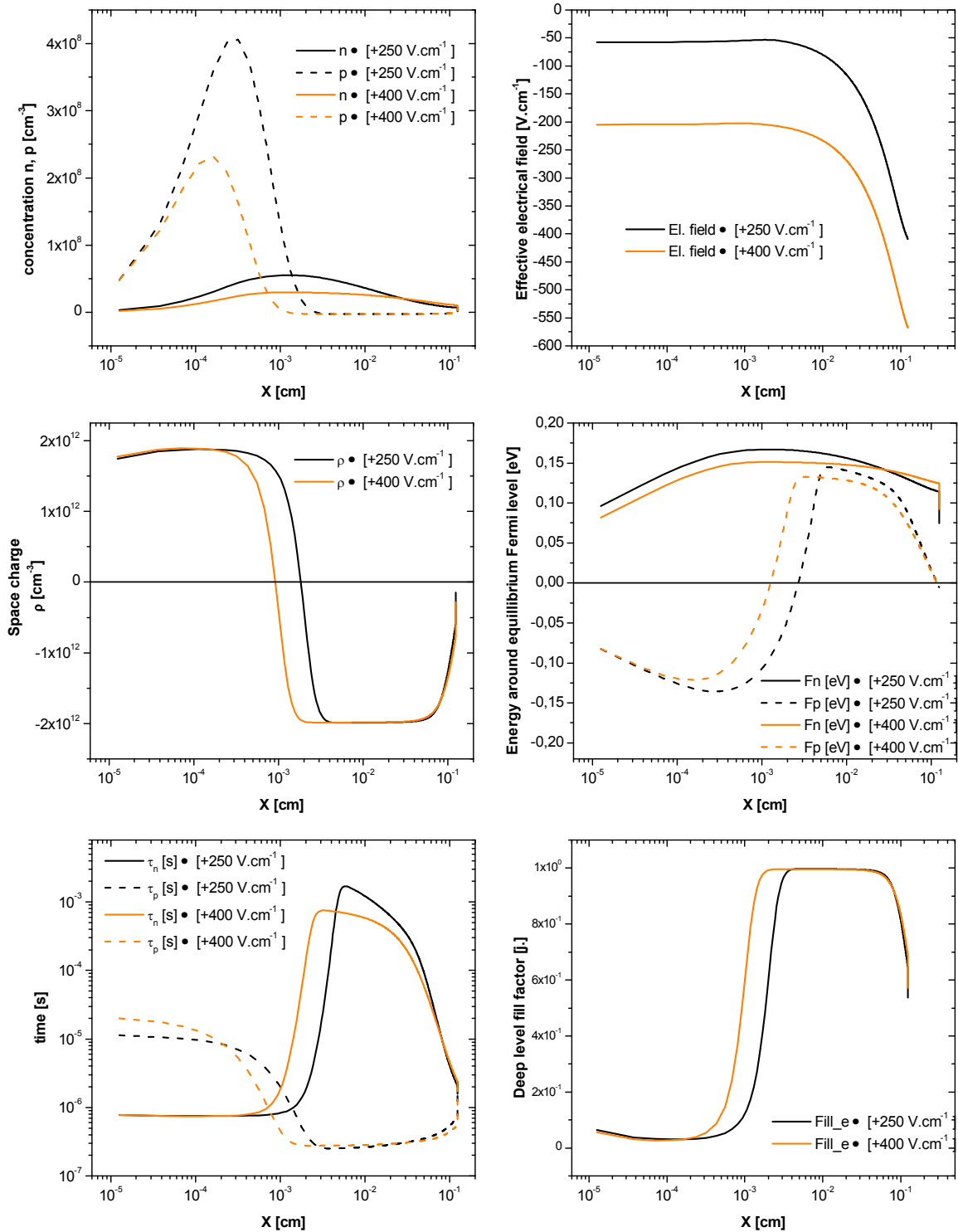
Fig. 6-31
Comparison of development electrical properties in the sample volume for 250 and 400V.cm⁻¹.

In the **Fig. 6-31** is shown distribution of concentration of free electrons and holes (n, p) in the sample. In our case of absorption coefficient 5000cm^{-1} most photons are absorbed in the thin front layer and generate electron-hole pairs. Holes are attracted by the front negative contact or recombine with electrons. Distribution of space charge (ρ) shown in **Fig. 6-31** reveals that whole sample except of the front thin layer is charged by the negative charge. This is due to capturing of free electrons, drifted to back positive contact, by the deep level. This implies that screening potential of space charge acts against influence of the applied electrical field.

It is clear from the **Fig. 6-30** that with a higher applied electric field the relative influence of space charge screening effect is decreased. From dependence of effective electrical field in **Fig. 6-31** we can explain why the influence of space charge is higher for lower applied fields. In the discussed case is minimal ratio of effective electric field in thin front layer of the sample vs. applied electrical field equal to one half in case of application 400V.cm^{-1} and only to one fifth in case of 250V.cm^{-1}.

Effectively lower electrical field screened by space charge causes that electrons are attracted to backside contact less than could be expected in the thin front layer. Slow drift motion of free electrons leads to their more intensive recombination and decreasing of their relaxation time in this front layer. We will observe this effect as photocurrent descent, for used photon energy opposite to case without space charge screening. This effect is stronger for higher absorption coefficient, where holes and electrons are separated in the front layer bellow illuminated contact already. Electron trapped on the center in back part of the sample has a low probability to recombine with hole. Only thermal holes and holes generated by the backside contact are there present. This is distinct from the deep level filling factor development in **Fig. 6-31**. With consideration of behavior of quasi-Fermi energy for electrons and holes shown in **Fig. 6-31** too, we can claim that centers on the deep level in the front thin layer act as recombination centers and centers in the back bulk part act as trapping centers. In homogenously irradiated sample with lower absorption coefficient are electron-hole pairs generated in the whole sample and recombination process via the deep level centers is much more effective, is such case is influence of space charge screening substantially lower.

The experimentally observed shift of the photocurrent (PC) peak at room temperature can be explained as an effect of screening of the applied electric field by space charge accumulated on deep levels. The fact, that the screening is strong at high α but weak at low α causes a shift of the PC peak to low α as a result of the space charge accumulation. We can summarize the basic analysis of the dependence of the position of PC peak on α as follows: the peak is shifted to higher α with increasing recombination and to lower α with increasing screening.

Summary of computed photocurrent peaks' position is shown in **Fig. 6-32**. The main photopeak shift is observed for concentrations $N_{deep} \sim 2 \times 10^{12}$-$1 \times 10^{13}$cm^{-3}. This is in very good agreement with our estimation about deep level concentration from measurement of Lux-Ampere characteristics. Negligible photopeak movement is observed for high 1×10^{13} and low 1×10^{12}cm^{-3} concentrations of deep levels. These two situations can be distinguished only by absolute value of photocurrent maximum. At low concentration of N_{deep} we will not observe any change of the photocurrent maximum. On the contrary at high concentration N_{deep} we can observe significant change. This corresponds to sample's Nr.5 experimental data shown in **Fig. 6-22**.
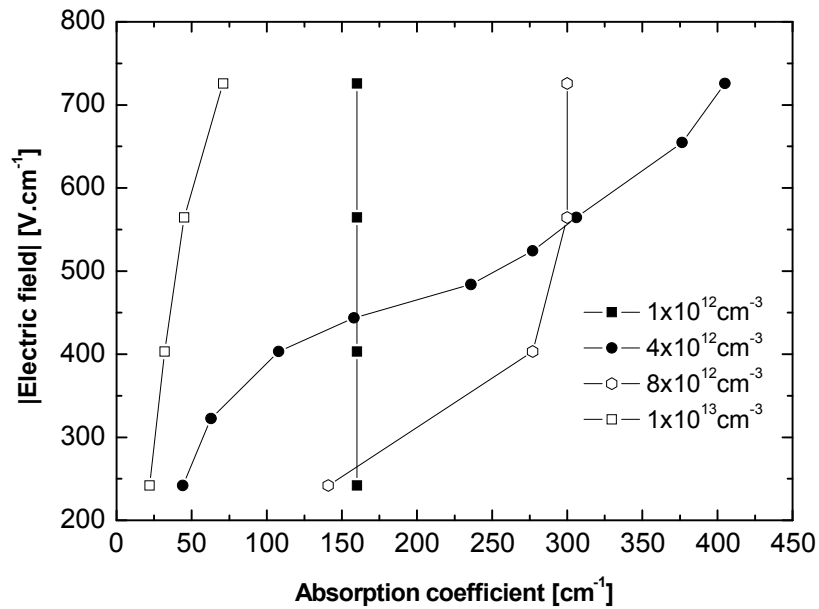
Fig. 6-32
Summary of the shift of the photoconductivity peak with the applied electric field

Conversion of the absorption coefficient used in previous work to photon energy can be done by following calibration, obtained from measurement of our set of samples. The measurement was done by P.Horodyský. Here the energy range 1.45-1.48eV corresponds to α at ~10-300cm^{-1}, which is in a good agreement with the position of the PC peak and its shift found in the theoretical analysis.

Fig. 6-33
Dependence of sample absorption coefficient on photon energy

7 Summary and conclusion

With aim to get more understanding about influence of deep levels on CdTe photoelectric properties, we performed measurem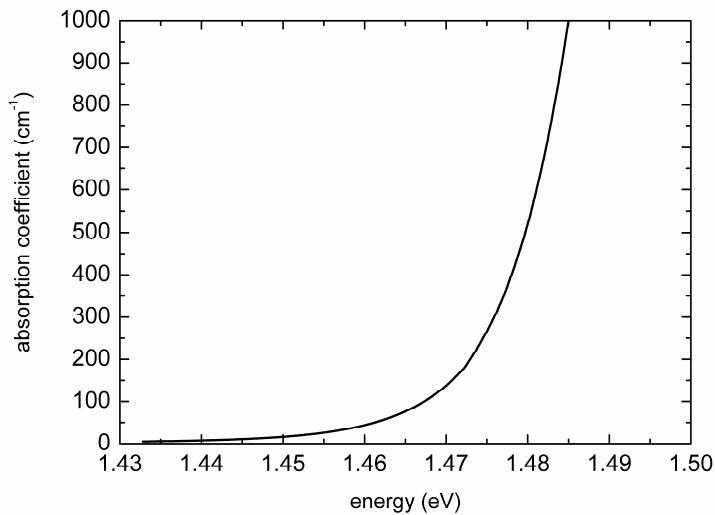ents of spectral dependences, Lux-Ampere and PICTS characteristics for several variously doped (Cl, Sn, and Ge) samples. Spectral and Lx-A measurements were performed at room temperature and low temperature 10K. In detail are discussed results for room temperature, where the numerical solution of photoelectric properties was done.

One of the most significant causes of the sublinear dependence Lux-Ampere characteristics is screening of space charge accumulated on deep levels. At low temperature 10K we acquire sublinear and over linear Lx-A dependences, such behavior is mentioned in literature too [58.].

Photocurrent peak shift to higher energies with applied electrical field was observed for room temperature. This effect was studied using numerical solution of drift-diffusion and Poisson equations. For typical midgap deep level concentration we achieved to explain PC peak shift as a result of screening of the applied electric field by accumulated space charge. This leads to higher recombination and PC peak shift to higher energies, because the effect is stronger for higher absorption coefficients. Photocurrent peak shift to lower photon energies was observed for low temperature 10K and simple model for this effect was introduced.

To obtain basic spectroscopic information about deep levels we performed PICTS experiment. For each studied sample we obtained several discrete levels, some of them corresponding with literature.

As upshot we can claim that space charge accumulated on deep level has significant influence to photoelectric properties. The influence of space charge on slopes of lux-ampere characteristics and on the shift of the main PC peak at room temperature can be used for a future development of a relatively simple method for a preliminary testing of CdTe samples in respect to their detection properties. The idea is based on an assumption, that in detector-grade samples a minimum concentration of deep levels accumulating space charge should be present. Therefore the simple model presented in Sec.4.6 cannot describe compensation processes leading to high resistivity CdTe and new approaches should be looked for.

The obtained experimental results and their theoretical evaluation open a possibility to develop a method of preliminary characterization of charge collection in high resistivity CdTe by photoelectric measurements based on the assumption, that good quality detector-grade material should contain only a minimum concentration of deep levels able to accumulate space charge.

8 References

[1] Y.Eisen, A.Shor, J.Cryst.Growth 184/185, (1998) 1302

[2] M. Squillante, L.Cirignano, R.Grazioso, Nucl.Instr.Meth. **A 458**, (2001) 288

[3] J. R. Heffelfinger, D. L. Medlin, H. Yoon, H. Hermon, and R. B. James, Proceedings of the SPIE, **40** (1997) 3115

[4] A.Zumbiehl, M.Hage-Ali, M.Ayoub, R.Regal, J.M.Koebel, P.Siffert, IEEE Trans.Nucl.Sci. **49**, (2002) 1254

[5] G.F.Neumark. "Defects in wide band gap II-VI crystals", Mater.Sci.Eng. **R21**, (1997) 1

[6] R. Grill, A. Zappettini, Progress in Crystal Growth and Characterization of Materials **48/49** (2004) 209

[7] M.A. Berding, Phys. Rev. B **60** (1999) 8943

[8] M.A. Berding, Private communications, 2000

[9] P. Emanuelsson, P. Omling, B.K. Meyer, M.Wienecke, M.Schenk, Phys. Rev B 47 (1993) 15578

[10] W. Stadler, D.M. Hofmann, B.K. Meyer, R. Krause-Rehberg, A. Polity, Th. Abgarjan, M. Salk, K.W. Benz, M. Azoulay, Acta Phys. Pol. **A 88** (1995) 921.

[11] A. Castaldini, A. Cavallini, B. Fraboni, P. Fernandez, J. Piqueras, J. Appl. Phys. **83** (1998) 2121.

[12] Y.C. Chang, R.B. James, in: R.B. James, R.C. Sherato (Eds.), Hard X-ray, Gamma-ray and Neutron Detektor Physics and Applications, Vol. **3768,** SPIE, Bellingham, WA (Phys. Rev. B), 1999, p. 381.

[13] M.A. Berding, Appl. Phys. Lett. **74** (1999) 552.

[14] Z.C. Huang, E. Eissler, C.R. Wie, Nucl. Instrum. Methods **B 100** (1995) 507.

[15] C. Szeles, Y.Y. Shan, K.G. Lynn, A.R. Moodenbaugh, E.E. Eissler, Phys. Rev. **B 55** (1997) 6945.

[16] M. Hage-Ali, P. Siffert, Semiconductors for room temperature nuclear detector applications, in: T.E. Schlesinger, R.B. James (Eds.), Semiconductors and Semimetals, Vol. 43, Academic Press, New York, 1995, p. 219.

[17] P.Y. Chian, J.H. Chen. Journal of Applied Physics **67**(5): (1989) 2475-2481.

[18] C. Corbel, L. Baroux, F.M. Kiessling, C. Gely-Sykes, R. Triboulet, Mater. Sci. Eng. **B 16** (1993) 134.

[19] F. Debbag , G.Bastide, M. Rouzeyre, Solid State Communications **67** (1): 1988

[20] M. Fiederle, D. Ebling, C. Eiche, D.M. Hofmann, M. Salk, W. Stadler, K.W. Benz, B.K. Meyer, J. Cryst. Growth **138** (1994) 529.

[21] Raychaudhuri et al., Journal of Applied Physics **55**(10): (1983) 3605

[22] E. Molva, J.P. Chamonal, J.L. Pautrat, Phys. Stat. Sol. (b) **109** (1982) 635.

[23] E. Molva, J.M. Francou, J.P. Pautrat, K. Samindayar, L.S. Dang, J. Appl. Phys. **56** (1984) 2241

[24] G. Hendorfer, G. Brunthaler, W. Jantsch, J. Reisinger, H. Sitter, J. Cryst. Growth **86** (1988) 497.

[25] M. Godlewski, J.M. Baranowski, Phys. Stat. Sol. (b) **97** (1980) 281.

[26] J.E. Toney, B.A. Brunett, T.E. Schlesinger, E. Cross, F.P. Doty, R.B. James, Mater. Res. Soc. Symp. Proc. **487** (1998) 59.

[27] A. Sarem, B.A. Orlowski, S. Kuzminski, Acta Phys. Pol. **A 79** (1991) 183.

[28] W. Jantsch, G. Brunthaler, G. Hendorfer, Mater. Sci. Forum 10±12 (1986) 515.

[29] P. Moravec, M. Hage-Ali, L. Chibani, P. Siffert, Mater. Sci. Eng. **B 16** (1993) 223.

[30] K. Lischka, G. Brunthaler, W. Jantsch, J. Cryst. Growth **72** (1985) 355.

[31] V.G. Deybuk, et al., Izv. Vuzov. Fizika **4** (1982) 24.

[32] P.I. Babii, V.V. Slynko, Yu.P. Gnatenko, P.N. Bukivskii, M.I. Llashchuk, O.A. Parfenyuk, Sov. Phys. Semicond. **24** (1990) 904.

[33] A. Zerrai, G. Bremond, J. Appl. Phys. **84** (1998) 5554.

[34] P. Christman, B.K. Meyer, J. Kreissl, R. Schwarz, K.W. Benz, Physical Review B **53**, (1996) 3634

[35] M.J. Caldas, Z. Fazzio, Z. Zunger, Appl. Phys. Lett. **45** (1984) 671.

[36] Kasherninov, PG, Matyukhin, DG, Sladkova, VA, Sov Phys Semicond. **14** (7): (1980) 763

[37] J.Franc, M.Fiederle, V.Babentsov, A.Fauler, K.W.Benz, James R., J. Electron. Mater **32** (7): (2003) 772

[38] M. Fiederle, V.Babentsov, J.Franc, A.Fauler, K.W.Benz, James R.B and Cross E, J.Cryst.Growth **243:** (2002), 77

[39] R.Grill, J.Franc, P.Hőschl, I.Turkevych, E.Belas, P.Moravec, IEEE Tranc.Nucl.Sci. **52**, (2005) 1925

[40] X. Mathew, Energy Materials & Solar Cells **76**: (2002) 225-242.

[41] G.M.Khattak and C.G.Scott. Journal Physics **3**: (1991) 8619

[42] R.E.Kremer, W. B. Leigh. Journal of Crystal Growth **86**: (1988) 490-496.

[43] J.M. Francou, K. Saminadayar, J.L. Pautrat, Phys. Rev. **B 41** (1990) 12035.

[44] E. Molva, K. Saminadayar, J.L. Pautrat, E. Ligeon, Solid State Commun. **48** (1983) 955.

[45] C.H. Park, D.J. Chadi, Phys. Rev. **B 52** (1995) 11884.

[46] D.M. Hofmann, P. Omling, H.G. Grimmeiss, B.K. Meyer, K.W. Benz, D. Sinerius, Phys. Rev. **B 45** (1992) 6247.

[47] T. Ido, A. Heurtel, R. Triboulet, Y. Marfaing, Journal of Phys. and Chem. Solids, **48** (9): (1987) 781

[48] E. Molva, J.L. Pautrat, K. Saminadayar, G. Milchberg, N. Magnear, Phys. Rev. **B 30** (1984) 3344.

[49] Y. Marfayng, Handbook od semicond, vol 2., (1980) 418-445

[50] W. Shockley and W.T Read, Phys. Rev. **87** (1952) 835

[51] J.C.Balland, J.P.Zielinger, M.Tapiero, J.G.Gross and C.Noguet. Applied Physics **19:** (1986) 71

[52] A. Rose – Concepts in photoconductivity and allied problems, Robert E.Krieger publishing, Huntington, NewYork, (1978) 34

[53] Toušek, J. Fotoelektrické jevy v polovodičích. Praha, Univerzita Karlova v Praze - SPN. (1977)

[54] H.B. de Vore, Phys. Rev 102 (1956) 86

[55] R.Grill, J.Franc, I. Turkevych, P. Höschl, Belas E., and P.Moravec. J. Electron. Mater **34** (2005) 939.

[56] L. Votoček, Diplomová práce, Fyzikální Ústav, MFF UK (2003), 95

[57] M. Tapiero, N.Benjelloun, J.P. Zielinger, S. El. Hams, and C. Noguet. J. Appl. Phys **64** (8), (1988) 4006

[58] R.H. Bube, Photoconductivity of solids, John Willey publishing, New York: (1960) 344

[59] J.Franc, P.Horodyský, E.Belas, V.Linhart, S.Pospíšil and R.Grill. IEEE Transactions of Nuclear Science **52**(5): (2005) 1956

9 Appendix

Table XI - List of notification of parameters user in this study

Symbol	Description	Unit
ρ	charge density	cm^{-3}
n	electron density	cm^{-3}
p	hole density	cm^{-3}
v_t	thermal velocity of electrons	$cm.s^{-1}$
E	electric field	$V.cm^{-1}$
φ	potential	V
E_i	intrinsic energy	eV
F_p	electron quasi-Fermi energy	eV
F_p	hole quasi-Fermi energy	eV
J_n	electron current density	$s^{-1}.cm^{-2}$
J_p	hole current density	$s^{-1}.cm^{-2}$
S_n	capture coefficient for electrons	cm^2
S_p	capture coefficient for holes	cm^2
I_{PC}	photocurrent density	$A.cm^{-2}$
t	time	s
τ	relaxation time	s
N_V	effective density of states in conduc. band	cm^{-3}
N_C	effective density of states in valence band	cm^{-3}
N_{deep}	deep level concentration	cm^{-3}
N_{fot}	photon flux	$s^{-1}.cm^{-2}$